Structure and function of the ROR2 cysteine-rich domain in vertebrate noncanonical WNT5A signaling

Samuel C. Griffiths[1†#], Jia Tan[2†], Armin Wagner[3], Levi Blazer[4], Jarret J. Adams[4], Srisathya Srinivasan[2], Shayan Moghisaei[2], Sachdev S. Sidhu[4], Christian Siebold[1*], Hsin-Yi Henry Ho[2*]

[1]Division of Structural Biology, Wellcome Centre for Human Genetics, University of Oxford, United Kingdom
[2]Department of Cell Biology and Human Anatomy, University of California, Davis, United States
[3]Science Division, Diamond Light Source, Harwell Science and Innovation Campus, Didcot, United Kingdom
[4]School of Pharmacy, University of Waterloo, Canada
[#]Current address: Evotec (UK) Ltd., 90 Innovation Drive, Milton Park, Abingdon OX14 4RZ, UK

†co-first authors
*co-corresponding authors

Abstract

The receptor tyrosine kinase ROR2 mediates noncanonical WNT5A signaling to orchestrate tissue morphogenetic processes, and dysfunction of the pathway causes Robinow syndrome, Brachydactyly B and metastatic diseases. The domain(s) and mechanisms required for ROR2 function, however, remain unclear. We solved the crystal structure of the extracellular cysteine-rich (CRD) and Kringle (Kr) domains of ROR2 and found that, unlike other CRDs, the ROR2 CRD lacks the signature hydrophobic pocket that binds lipids/lipid-modified proteins, such as WNTs, suggesting a novel mechanism of ligand reception. Functionally, we showed that the ROR2 CRD, but not other domains, is required and minimally sufficient to promote WNT5A signaling, and Robinow mutations in the CRD and the adjacent Kr impair ROR2 secretion and function. Moreover, using function-activating and -perturbing antibodies against the Frizzled (FZ) family of WNT receptors, we demonstrate the involvement of FZ in WNT5A-ROR signaling. Thus, ROR2

acts via its CRD to potentiate the function of a receptor super-complex that includes FZ to transduce WNT5A signals.

Introduction

ROR proteins make up an important branch of the receptor tyrosine kinase (RTK) superfamily, conserved from sponges to humans. Originally identified as orphan receptors based on sequence homology to other RTKs (hence the name Receptor tyrosine kinase-like Orphan Receptor), work over the past two decades has elucidated a critical role of the ROR RTK family in mediating noncanonical WNT5A signaling (Oishi et al., 2003, Mikels and Nusse, 2006, Ho et al., 2012, Green et al., 2008). Unlike canonical WNTs, which signal through β-catenin-dependent transcription to regulate cell proliferation and tissue fate, WNT5A signals noncanonically through β-catenin-independent mechanisms to induce cytoskeletal rearrangements and tissue morphogenetic changes (Konopelski Snavely et al., 2023, Moon et al., 1993, Veeman et al., 2003). The pathway is also of clinical significance, as mutations in WNT5A, the ROR family member ROR2, and the downstream signal transducers Dishevelled 1 (DVL1) and DVL3 have been reported to cause Robinow syndrome (RS), a congenital disorder characterized by systemic tissue shortening defects, including dwarfism, mesomelic limb shortening, brachydactyly, genitourinary defects, cleft palate and other craniofacial dysmorphisms (Person et al., 2010, Afzal et al., 2000, van Bokhoven et al., 2000, Bunn et al., 2015, White et al., 2015, White et al., 2016), and a distinct cohort of ROR2 missense mutations cause brachydactyly type B (BDB) (Oldridge et al., 2000, Schwabe et al., 2000). Moreover, elevated expression of ROR1 or ROR2 correlates with increased cancer metastatic potentials,

and several anti-ROR therapies are currently in various stages of development (Rebagay et al., 2012, Kipps, 2022). The etiological mechanisms of these mutations, however, remain largely uncharacterized. Thus, a greater understanding of ROR receptor function is important from both basic science and medical perspectives.

ROR receptors are type-I transmembrane proteins with a single-pass transmembrane (TM) helix linking extracellular and intracellular regions. The extracellular region of vertebrate ROR proteins consists of an immunoglobulin (Ig) domain, a Frizzled (FZ)-like cysteine-rich domain (CRD) and a Kringle domain (Kr). The intracellular region includes a tyrosine kinase domain (Tk) and a serine/threonine/proline-rich domain (S/T/P) (Minami et al., 2010, Green et al., 2008). The specific requirement of these domains in WNT5A signaling remains controversial. Early genetic studies in *C. elegans* showed that only the CRD and the transmembrane (TM) helix are essential for the function of the nematode ROR homolog Cam-1 in cell migration, which raised the possibility that Cam-1 may not act as a typical RTK and may instead regulate the spatial distribution of WNT ligands (Kim and Forrester, 2003). Experiments in vertebrate systems, however, largely suggest that ROR proteins act as *bona fide* WNT signaling receptors and that this function requires other domains of ROR proteins, including the intracellular domains (DeChiara et al., 2000, Oishi et al., 2003, Mikels and Nusse, 2006). However, due to the historical lack of tractable assays to directly measure ROR activity, the precise requirement of vertebrate ROR proteins in noncanonical WNT5A signaling has not been systematically examined.

The CRD is of broader interest because it is not only conserved within the ROR family but also among other important receptor classes where the domain mediates ligand and/or co-

factor binding through a signature hydrophobic groove or pocket (Bazan and de Sauvage, 2009). For instance, the CRD of the classical WNT receptor FZ interacts with the palmitoleate moiety of WNT ligands directly through this groove (Janda et al., 2012). Free fatty acids have also been observed to interact in the same fashion (Nile et al., 2017). Moreover, the CRD of the Hedgehog signal transducer and GPCR Smoothened (Smo) binds cholesterol through an analogous hydrophobic pocket (Byrne et al., 2016). Because the CRD of ROR2 was previously implicated in WNT5A binding (Oishi et al., 2003, Mikels and Nusse, 2006), and shares a high degree of amino acid sequence similarity with the FZ CRD (Xu and Nusse, 1998, Saldanha et al., 1998), it is assumed that it possesses a similar hydrophobic groove via which it interacts with WNT5A. However, this hypothesis remains untested, as the requirement of the vertebrate ROR2 CRD in WNT5A signaling and its atomic structure have not been determined.

In this study, we determined the crystal structure of the ROR2 CRD and Kr domains. Remarkably, we found that the two domains share an extended interface and that the ROR2 CRD lacks the characteristic hydrophobic groove/pocket for interacting with lipids. The latter observation suggests that the ROR2 CRD cannot mediate high-affinity interaction with the palmitoleate group of WNT5A. To further probe the requirement of the ROR2 CRD in WNT5A signaling, we developed a functional complementation assay in *Ror1/Ror2* double knockout mouse embryonic fibroblasts (MEFs) and showed that the ROR2 CRD is required and minimally sufficient to mediate WNT5A-ROR signaling. We implicated the FZ family in the pathway by showing that WNT5A directly interacts with the CRD of multiple FZ proteins, and that synthetic immunoglobulins that bind the FZ CRDs can potently activate or inhibit WNT5A-ROR signaling depending on their valency. Lastly, we demonstrated that several Robinow patient mutations in

the CRD and Kr domains impair ROR2 secretion and function, presumably by disrupting the proper folding of these domains. Collectively, the study provides structural and functional insights into ROR2 function and supports a model in which ROR2 acts through its CRD to promote FZ-dependent WNT5A signaling.

Results

The structure of the ROR2 CRD and Kr domains

To determine the structure of the ROR2 CRD, we expressed a range of constructs comprising the full-length human ROR2 extracellular region (Figure 1A). Analysis of construct secretion revealed that deletion of the Kr domain severely impacted the yield of ROR2 constructs (Figure 1-figure supplement 1A), and therefore the full extracellular region (ECD) and CRD-Kr were selected for large-scale expression and purification (Figure 1-figure supplement 1B and C).

We determined a crystal structure of the ROR2 CRD-Kr tandem domain construct at a resolution of 2.48 Å via a platinum single-wavelength anomalous dispersion experiment coupled with molecular-replacement (MR-SAD) (Supplementary File 1, Figure 1-figure supplement 1D-H; see experimental procedures for details). The CRD comprises 5 α-helices (α1-5) and a single β-sheet (strands β1 and β2), while the Kr domain presents a characteristic lack of secondary structure, displaying a single β-sheet (strands β3 and β4) (Figure 1B, left-hand panel). The CRD is stabilized by 5 disulfide bonds: one located between β1 and a loop extending from helix α2 (I), a second linking α2 and the loop preceding longest helix α1 (II), a third between helix α2 and the loop between helices α3/4 (III), a fourth between long loops following helices

α2 and α3 (IV), and the fifth between helix α3 itself and the loop extending from α5 (V). The Kr domain is stabilized by 2 disulfide bonds (VI and VII) that are found within the core of the Kr domain. A structured linker is observed between both domains, containing one additional free cysteine (C316). This is positioned in proximity to the C-terminus of our expression construct, which contains one additional cysteine residue (C394), unresolved in our ROR2 CRD-Kr crystal structure (Figure 1-figure supplement 1D).

Overall, the CRD and Kr domains form an associated structural unit (Figure 1B, right-hand panel). A contact interface is observed between the two domains and is dominated by van der Waals interactions, with two hydrogen bonds present (Figure 1C). The domains share a small interfacial area of 559 $Å^2$, with a reasonable shape complementarity score (0.7) (Lawrence and Colman, 1993). The structure of Kr in the CRD-Kr tandem domain closely resembles that previously described for the isolated human ROR1 and ROR2 Krs (Goydel et al., 2020, Guarino et al., 2022) (Figure 1-figure supplement 2A). Shi et al. recently described the structure of the extracellular region of the Drosophila ROR2 homolog Nrk, which consists of a CRD and a Kr domain (Shi et al., 2021). There is also a high degree of structural conservation between the ROR2 and Nrk Kr domains (Shi et al., 2021) (Figure 1-figure supplement 2A). Kr domains are generally observed to constitute protein-protein interfaces within multi-domain proteins (Deguchi et al., 1997, Ultsch et al., 1998, Zebisch et al., 2016), suggesting that the ROR2 Kr domain acts to stabilize the CRD (Figure 1-figure supplement 1A). Interestingly, while the CRD and Kr domains of Nrk also form an associated structural unit (Shi et al., 2021), and the secondary structural elements of these domains are highly conserved between human and Drosophila (Figure 1-figure supplement 2B), the spatial arrangement of CRD and Kr in ROR2 is

substantially different from that in Nrk (Figure 1-figure supplement 2C). Correspondingly, the CRD-Kr interfaces in ROR2 and Nrk are also structurally distinct (Figure 1-figure supplement 2C).

The full-length ROR2 ECD is monomeric in solution at concentrations as high as 48 µM (Figure 1-figure supplement 1B and C), indicating that the CRD does not mediate dimerization as has been suggested for other related FZ-type CRDs (Dann et al., 2001), and also suggesting that the Ig and Kr domains do not facilitate oligomerization. We conducted small angle X-ray scattering experiments with in-line size exclusion chromatography (SEC-SAXS) experiments using the full-length ROR2 ECD (Figure 2-figure supplement 1). The CRD-Kr arrangement observed in the crystal structure is conserved in solution (Figure 2-figure supplement 1A), while the N-terminal Ig domain is flexible relative to the CRD-Kr domain unit (Figure 2-figure supplement 1B), as predicted from the 15-residue linker between domains. Additionally, SAXS does not suggest that the ROR2 ECD forms a dimer in solution; however, we cannot exclude the possibility that the transmembrane helix and/or the intracellular domain could mediate dimerization. Structurally, the ROR2 CRD is evolutionarily related to other FZ-type 'groove-containing' CRDs (Nachtergaele et al., 2013), such as MuSK and FZ8 (Figure 1D and Supplementary File 2) (Stiegler et al., 2009, Dann et al., 2001, Janda et al., 2012), as well as the cholesterol-binding Hedgehog signal transducer Smo (Byrne et al., 2016). These are structurally distinct to the 'pocket-type' CRDs such as NPC1 and RFBP, which bury their physiological ligands in deep cavities (Bazan and de Sauvage, 2009).

Structural analysis of ROR2 CRD function

The FZ-type CRDs from both FZ8 and Smo exhibit shallow hydrophobic grooves for the binding

164 of palmitoleate or cholesterol, respectively (Janda et al., 2012, Byrne et al., 2016) (Figure 2A-C).
165 One general characteristic differentiating this sub-family of CRDs from the 'pocket-type' sub-
166 family is that grooves are structurally conserved when ligand-free (Figure 2A and B), with
167 minimal structural rearrangement occurring upon ligand binding (Dann et al., 2001, Janda et al.,
168 2012, Nachtergaele et al., 2013, Byrne et al., 2016). Despite structural conservation with other
169 FZ-type receptors, the ROR2 CRD does not contain a visible hydrophobic groove pre-formed for
170 ligand recognition (Figure 2D). A structure-based sequence alignment shows that the ROR2 CRD
171 has evolved an additional helical insertion (α5) relative to the FZ8 CRD (Figure 2E). Structural
172 superposition of the ROR2 CRD with the FZ8:WNT-palmitoleate binary complex (Janda et al.,
173 2012) shows that this helical insertion blocks exposure of any possible palmitoleate-binding
174 groove (Figure 2F, Figure 1-figure supplement 1F-H). This observation is therefore incompatible
175 with a direct binding event occurring between the ROR2 CRD and the WNT5A palmitoleate
176 moiety, suggesting that the high affinity 'site 1' WNT5A interaction must occur either via a
177 different site on the CRD or through a separate co-receptor(s), or require structural
178 rearrangements as-yet not observed for groove-containing FZ-CRDs.

179 The structure of the Nrk CRD revealed a deeply buried fatty acid (Shi et al., 2021),
180 whereas no bound lipid, nor an internal space that could potentially accommodate it, was
181 observed in our human ROR2 CRD structure (Figure 2D and F). Structural comparison of the
182 ROR2 and Nrk CRDs showed that the region of Nrk that interacts with the lipid does not
183 superpose well with the analogous region in ROR2 (Figure 2-figure supplement 2). Notably,
184 residue K170 of Nrk that interacts with the head group of the fatty acid is absent in ROR2
185 (Figure 1-figure supplement 2). Another basic side chain that contacts the head group of the

lipid in Nrk is R179 – this residue is conserved in ROR2 (R280), but its side chain protrudes into solution (Figure 2-figure supplement 2). It is noteworthy that in FZ-CRD structures for which apo- and lipid-bound structures are available (e.g. FZ4), major structural rearrangements within the CRD are not observed upon ligand recognition (Shen et al., 2015, DeBruine et al., 2017). Taken together, these observations suggest that ROR2 is unlikely to bind an internally buried free fatty acid analogous to that observed in Nrk.

Functional requirement of the ROR2 CRD in WNT5A signaling

We next examined the requirement of the ROR2 CRD, as well as that of other ROR2 domains, in WNT5A signaling. We first developed a central rescue paradigm that allowed us to exogenously express various ROR2 mutant proteins in *Ror1/Ror2* double knockout (ROR KO) mouse embryonic fibroblasts (MEFs) and assess their ability to restore WNT5A signaling (Figure 3A). For these experiments, we isolated primary MEFs from E12.5 *Ror1*$^{f/f}$*; Ror2*$^{f/f}$*; CAG-CreER* embryos that carry conditional (floxed, or *f*) alleles of *Ror1* and *Ror2*, as well as a *CreER* transgene driven by the ubiquitously expressed *CAG* promoter (Susman et al., 2017, Hayashi and McMahon, 2002). E12.5 was chosen because we previously showed that MEFs from this embryonic age are particularly responsive to WNT5A-ROR signaling (Susman et al., 2017, Konopelski, 2021). To enable long-term genetic manipulations, we immortalized the MEFs (called iMEFs) via Cas9/CRISPR-mediated ablation of the *Tp53* gene (Dirac and Bernards, 2003). To allow quantitative measurement of WNT5A-ROR signaling, we further engineered a GFP-Pdzrn3 degradation reporter construct into the iMEFs. We previously reported that activation of WNT5A-ROR signaling induces the proteasomal degradation of the downstream effector

208 protein Pdzrn3, and that this regulation could be quantified using the GFP-Pdzrn3 reporter in
209 live cells via flow cytometry (Konopelski, 2021). We next treated the iMEF reporter cells with 4-
210 hydroxy-tamoxifen (4OHT), which activates the genetically encoded CreER protein to induce
211 excision of the floxed *Ror1* and *Ror2* alleles. Lastly, to compare the activity of wildtype (WT)
212 ROR2 versus its mutant derivatives, we developed a lentivirus-based gene replacement strategy
213 that allowed the stable expression of ROR2 "rescue" constructs (Figure 3A-C). WNT5A dose-
214 response analysis comparing ROR conditional KO (cKO) reporter cells versus ROR KO cells (i.e.
215 cKO cells treated with 4OHT) showed that loss of ROR1 and ROR2 expression substantially
216 decreased WNT5A signaling across all WNT5a doses tested, and that this deficit can be fully
217 rescued by the expression of an exogenous WT ROR2 construct (Figure 3C). Interestingly, ROR
218 KO reporter cells without any ROR2 rescue still retained some basal WNT5A signaling activity,
219 which remained dose-dependent with respect to WNT5A concentration (Figure 3C). This
220 observation indicates that, while ROR receptors play an important role in promoting WNT5A
221 signaling, additional receptor(s) exist in these cells to transmit the WNT5A signal.

222 To systematically identify the domain(s) of ROR2 required for WNT5A signaling, we
223 generated a series of ROR2 domain truncation mutants based on the folded domain boundaries
224 identified by our crystal structure (Figure 3D) and assessed their ability to restore WNT5A
225 signaling in the iMEF signaling rescue assay. Immunoblotting confirmed that the mutant
226 proteins were expressed at levels comparable to the WT ROR2 rescue construct (Figure 3E). Cell
227 surface staining using the Flag epitope tag fused to the N-terminus of the WT and mutant ROR2
228 rescue constructs further confirmed that these constructs are expressed on the plasma
229 membrane at comparable levels (Figure 3-figure supplement 1A). Signaling analysis using the

230 GFP-Pdzrn3 degradation reporter revealed that the two ROR2 mutants lacking the CRD (ΔCRD
231 and ΔCRD-Kr) completely failed to restore WNT5A-induced degradation of the GFP-Pdzrn3
232 reporter (Figure 3F). The same defects were observed when we assayed DVL2 phosphorylation
233 as an independent readout of WNT5A-ROR signaling (Ho et al., 2012) (Figure 3-figure
234 supplement 2A-B). These results thus established that the CRD is essential for WNT5A signaling.
235 Surprisingly, all other mutants in the series, including one lacking almost the entire intracellular
236 region (ΔICD), still retain significant signaling capability, indicating that only the CRD is
237 indispensable for the core function of ROR2 in promoting WNT5A signaling (Figure 3F, Figure 3-
238 figure supplement 2A-B).

239 We next assessed the sufficiency of the ROR2 CRD in mediating WNT5A signaling. We
240 engineered a chimeric construct (mini-ROR2) in which the isolated ROR2 CRD and Kr tandem
241 domains are fused to a generic transmembrane helix derived from the unrelated protein CD45
242 (Chin et al., 2005), followed by a small, intracellular juxtamembrane fragment (Figure 3G).
243 Immunoblotting and cell surface staining experiments confirmed the protein and cell surface
244 expression of mini-ROR2 (Figure 3H and Figure 3-figure supplement 1B). Signaling analyses by
245 GFP-Pdzrn3 reporter degradation and DVL2 phosphorylation showed that mini-ROR2 can
246 substantially rescue WNT5A signaling (Figure 3I, Figure 3-figure supplement 2C-D). This
247 experiment, taken together with the truncation analysis, established that the ROR2 CRD is
248 required and minimally sufficient to support the function of ROR2 in WNT5A signaling.

249

250 **Role of FZ receptors in WNT5A-ROR signaling**

Based on our observations that 1) the ROR2 CRD lacks the hydrophobic groove that binds to the lipid modification of WNT5A (Figure 2D and F), 2) iMEFs lacking both ROR1 and ROR2 still retain some signaling activity (Figure 3C), and 3) ROR2 lacking the intracellular region can still signal (Figure 3F), we postulated that ROR2 cannot by itself function as the signaling receptor for WNT5A; instead, it likely facilitates the signaling function of another receptor(s). Members of the FZ family, particularly the FZ1, FZ2 and FZ7 subfamily, are plausible candidates, as numerous previous studies have implicated them in aspects of noncanonical WNT5A signaling (Oishi et al., 2003, Sato et al., 2010, Grumolato et al., 2010, Yu et al., 2012, Konopelski, 2021). Furthermore, a human mutation in FZ2 was recently identified in Robinow syndrome patients (White et al., 2018). To explore the role of the FZ family in WNT5A-ROR2 signaling, we first compared the ability of the ROR2, FZ2 and FZ7 CRDs to bind WNT5A. We expressed and purified these CRDs as secreted immunoglobulin Fc domain fusion constructs from HEK293T cells, followed by *in vitro* pulldown assays using purified recombinant WNT5A. The experiment showed that WNT5A can interact with all three CRDs tested, and that the binding affinity appears to be higher for the FZ2 and FZ7 CRDs than for the ROR2 CRD (Figure 4A). This finding is consistent with our structural data and with previous binding studies (Oishi et al., 2003, Mikels and Nusse, 2006, Sato et al., 2010), and suggests that despite lacking the hydrophobic groove, the ROR2 CRD can still bind WNT5A via a presumably lipid-independent manner.

To further test whether the binding interaction between WNT5A and the FZ CRD is important for signaling, we treated iMEF reporter cells with a synthetic monoclonal antibody, F2.A, that binds the CRD of six FZ family members, including FZ1, FZ2 and FZ7, and competes with WNTs for FZ binding (Pavlovic et al., 2018). We hypothesized that if FZs participate in

WNT5A-ROR2 signaling, then treatment with this antibody should block the ability of WNT5A to induce signaling. Surprisingly, we found that F2.A, in its bivalent IgG form and in the absence of any WNT5A, strongly induced GFP-Pdzrn3 reporter degradation, as well as DVL2 phosphorylation, in ROR cKO iMEFs, ROR KO iMEFs and WT ROR2 rescued iMEFs (Figure 4B; Figure 4-figure supplement). An independent bivalent IgG F1.C, which specifically targets the CRD of FZ1, similarly induced GFP-Pdzrn3 degradation and DVL2 phosphorylation (Figure 4B; Figure 4-figure supplement). Dose-response analyses of the F2.A and F1.C IgGs showed that these antibodies are highly potent in inducing Pdzrn3 degradation, with the respective EC_{50} values of 0.30 nM and 7.0 nM (Figure 4C and 4D). Moreover, we observed that at post-saturating concentrations, both IgGs exhibited reduced activity (Figure 4C and 4D), suggesting that they might function by inducing FZ dimerization. To further explore this idea and the functional role of FZs in WNT5A signaling, we tested the monovalent antigen-binding fragment (Fab) of F2.A and found that it not only lost the ability to induce signaling on its own (Figure 4E), possibly because it could no longer dimerize FZs, but instead, acted as a potent antagonist of WNT5A-dependent pathway activation (Figure 4F), presumably by blocking the WNT5A-FZ CRD interaction. Altogether, these data support a model in which FZs function as the signaling receptors for WNT5A, and ROR2 acts through its CRD to enhance FZ function, possibly by promoting WNT5A-FZ interactions and/or FZ dimerization (Figure 6; see Discussion).

Robinow syndrome mutations in the ROR2 CRD and Kr domains compromise ROR2 trafficking to the cell surface

294 Of all the ROR2 domains, the CRD and Kr domains are most frequently mutated in Robinow
295 syndrome patients (Tufan et al., 2005, Afzal et al., 2000, Tamhankar et al., 2014, Mehawej et
296 al., 2012). Our structural and functional data suggest that these mutations would disrupt the
297 function of ROR2 in WNT5A signaling. To test this hypothesis, we expressed and characterized
298 five substitution mutations from Robinow patients that map to the CRD (C182Y, R184C, R189W,
299 C223Y, R272C) and two that map to the Kr domain (G326A and R366W), using the ROR KO iMEF
300 rescue system. Western analysis showed that all seven mutant proteins were expressed at
301 comparable levels as WT ROR2 (Figure 5A). In WNT5A signaling assays, we found that three of
302 the five CRD mutations (C182Y, R184C and C223Y) and both Kr mutations (G326A and R366W)
303 exhibited strongly reduced signaling capabilities (Figure 5B, Figure 5-figure supplement 1). The
304 remaining two mutants (R189W and R272C) exhibited milder but still statistically significant
305 signaling deficits (Figure 5B, Figure 5-figure supplement 1).

306 We noticed that the five mutants with severe signaling defects (C182Y, R184C, C223Y,
307 G326A and R366W) all exhibited increased gel mobility in western analysis (Figure 5A),
308 suggestive of possible defects in glycosylation/trafficking through the secretory pathway.
309 Correspondingly, the two mutants with milder signaling defects (R189W and R272C) showed a
310 partial increase in their gel mobility (Figure 5A). To assess the glycosylation state of the mutant
311 constructs, we conducted endoglycosidase H (Endo H) and Peptide-N-Glycosidase F (PNGase F)
312 sensitivity assays. Complex glycan modifications attached in the Golgi are resistant to Endo H,
313 whereas both pre- and post-Golgi glycan modifications are generally sensitive to PNGase F. This
314 analysis shows that C182Y, R184C, C223Y, G326A and R366W are fully sensitive to both Endo H
315 and PNGase F, indicating that these mutants fail to traffic to and beyond the Golgi (Figure 5C).

316 In contrast, R189W and R272C are partially resistant to Endo H but fully sensitive to PNGase F,
317 indicating that some of these proteins can traffic to and past the Golgi (Figure 5C). Lastly, we
318 conducted surface staining experiments using the Flag tag fused to the N-terminus of the
319 mutant constructs and found that C182Y, R184C, C223Y, G326A and R366W all fail to traffic to
320 the plasma membrane, whereas R189W and R272C are expressed on the cell surface (Figure 5-
321 figure supplement 2).

322 Further insights into the pathogenic mechanisms of Robinow mutations were obtained
323 from our structural analysis. C182Y and C223Y disrupt conserved cysteines in the CRD. Since our
324 structure showed that all 10 cysteines in the CRD are involved in disulfide bond formation
325 (Figure 1B), these mutations likely cause Robinow syndrome by destabilizing the core structure
326 of the CRD (Figure 5D-F). Two other mutations in the CRD (R184C and R272C) involve amino
327 acid substitution to cysteines. Since both residues are solvent exposed (Figure 5D-F), they may
328 form cryptic intramolecular disulfide bonds that disrupt the protein fold, or alternatively form
329 intermolecular disulfide bonds that cause inappropriate dimerization or oligomerization that
330 results in protein aggregation. Based on our signaling data (Figure 5B), R184C is likely more
331 prone to these perturbations than R272C. R189W showed the least functional deficit in our
332 assay system. It is possible that even a subtle signaling deficit is sufficient to disrupt embryonic
333 development and cause Robinow syndrome. Alternatively, R189W might be involved in other
334 aspects of ROR2 regulation not readily detected in our assay system.

335 Interestingly, the two mutations that map to the Kr domain (G326A and R366W) are
336 among the most detrimental (Figure 5B, Figure 5-figure supplement 1). Both of these mutations
337 are located near the CRD-Kr interface (Figure 5D and G). G326 is situated near the linker

338 between the CRD and Kr (Figure 5D and G), and therefore, substitution at this position may
339 open up the space between the two domains and expose hydrophobic residues to promote
340 protein aggregation, which in turn prevents trafficking out of the ER. Likewise, R366W may
341 disrupt the overall fold of Kr, or disrupt the interface between the CRD and Kr to destabilize the
342 CRD-Kr structural unit (Figure 5D and 5G). Together, these functional and structural analyses
343 provide new insights into the molecular mechanisms of Robinow pathogenesis.
344

345 **Discussion**

346 In this study, we used an integrated approach of structural biology, genetics, and pharmacology
347 to better understand the mechanism of WNT5A signal reception at the cell surface. We made
348 several key observations that substantially advance our current understanding of WNT5A
349 receptor function.

350 First, by solving the crystal structure of the ROR2 CRD, we made the surprising finding
351 that this domain lacks the characteristic hydrophobic groove that binds the acyl moiety of
352 WNTs and is thus incompatible with high affinity interaction with WNT ligands. Our binding
353 assay showed that the binding affinity between WNT5A and the ROR2 CRD indeed appears to
354 be weaker than that between WNT5A and FZ CRDs. These experimental data agree with the
355 modeling work by Janda and Garcia, which predicted that the ROR2 CRD might not possess the
356 hydrophobic groove to accommodate the lipid modification of WNTs (Janda and Garcia, 2015).
357 This also agrees with the published crystal structure of MuSK, which is related to ROR2 and also
358 lacks a hydrophobic groove in its CRD (Stiegler et al., 2009). The occlusion of the lipid/small
359 molecule-binding site in ROR2 is unexpected and of general interest because this site was

360 previously shown to play an important role not only for WNT-FZ binding and FZ dimerization
361 during canonical WNT signaling, but also for Smo function during Hedgehog signaling (Janda et
362 al., 2012, Byrne et al., 2016, Nachtergaele et al., 2013, Nile et al., 2017). As there is clear
363 evidence that the mammalian WNT5A is lipidated (Mikels and Nusse, 2006), our data raised the
364 question of which co-receptor(s) in the pathway, if not ROR, is responsible for high-affinity
365 WNT5A binding and signal transduction across the membrane. Though the exact identity of this
366 co-receptor remains to be determined, our work points to the FZ receptor family, as
367 experimental dimerization of FZ proteins using a highly specific bivalent IgG that binds the FZ
368 CRDs is sufficient to mimic WNT5A signaling, whereas monovalent Fab of the same antibody
369 inhibits the ability of WNT5A to initiate signaling. We therefore favor a model in which WNT5A
370 interacts with FZ with high affinity to transduce signals across the plasma membrane, either by
371 itself or in conjunction with another as-yet unidentified protein(s). The ROR2 CRD appears to
372 possess a low-affinity WNT5A binding site, possibly analogous to the low affinity "site 2"
373 observed in the WNT8-FZ8 complex (Janda et al., 2012). The ROR2 CRD could possibly
374 potentiate WNT5A signaling by enhancing the binding interaction between WNT5A and FZ via
375 the formation of a FZ:WNT:ROR2 super-complex (Figure 6). In this scenario, the WNT5A
376 palmitoleate modification engages the FZ groove as previously described ('site 1') (Janda et al.,
377 2012), whilst ROR2 binds at site 2 to further promote WNT5A recruitment to the receptor
378 complex, and/or recruit intracellular effectors of noncanonical WNT signaling. This model
379 further suggests that while the high-affinity WNT5A palmitoleate-FZ interaction may act as an
380 indiscriminate anchor to stabilize the overall receptor super-complex and initiate downstream
381 signaling, it is likely the low-affinity WNT5A-ROR2 CRD interaction that contributes to ligand-

receptor specificity for noncanonical WNT5A signaling. Lastly, it is also possible that ROR2 CRD can act by inducing an allosteric change in the structure of FZ to enhance FZ function or promote FZ dimerization that in turn increases FZ's affinity for WNT5A (Carron et al., 2003, Nile et al., 2017).

Second, we observed that ROR2 mutants lacking the intracellular domain (ΔICD and mini-ROR2) can still support WNT5A signaling. This is in-line with the idea that ROR2 itself is unlikely to be the signal-transmitting receptor for WNT5A, and that the cytoplasmic domain of ROR2 might have evolved to play a regulatory role, such as in receptor stability, signal amplification and/or termination. This idea is further supported by the observation that some residual signaling activity remains in cells lacking both ROR1 and ROR2 when stimulated with exogenously added WNT5A, and that the structure of the ROR2 kinase domain predicts it to be inactive (Artim et al., 2012). Collectively, these findings firmly established a co-requirement for both ROR and FZ activities in noncanonical WNT5A signal transduction. This model is also consistent with previous *in vivo* work showing that *Ror1/Ror2* double knockout mice phenocopy the characteristic tissue truncation phenotypes of *Wnt5a* KO mice, and that human mutations in *WNT5A*, *ROR2* or *FZ2* can all cause Robinow syndrome with similar developmental abnormalities (Nagasaki et al., 2018, White et al., 2018, Person et al., 2010, Afzal et al., 2000). Though several previous co-immunoprecipitation experiments have shown binding interactions between WNT5A and ROR2 (Oishi et al., 2003, Mikels and Nusse, 2006), between WNT5A and FZ family members (Sato et al., 2010), and between FZ and ROR proteins (Oishi et al., 2003), the biochemical details of these interactions remain to be characterized. In light of our present work, it is crucial to further define these interactions quantitatively in future studies and to

404 understand their functions in the context of a co-receptor super-complex. Nonetheless, our
405 results showing that ROR2 acts through its CRD to sensitize the function of FZs or a FZ-
406 containing receptor complex during WNT5A-ROR signaling form the foundation for future
407 studies.

408 Lastly, our work provides new insights into the molecular mechanisms of Robinow
409 pathogenesis. Using the gene replacement strategy in iMEFs, we were able to directly assay the
410 function of Robinow syndrome mutant variants under highly physiological conditions. We found
411 that nearly all of the mutants tested exhibited defects in their trafficking to the cell surface and
412 hence WNT5A signaling, and that mutating the cysteines required for disulfide bonds in the CRD
413 was not tolerated. Furthermore, by combining these functional data with our structural
414 analysis, we can classify the mutations based on their locations on the CRD-Kr structure and
415 infer potential underlying mechanisms of structural and signaling perturbation. We envision
416 that the experimental approach described in this study will serve as an important model for
417 interrogating other mutations in the pathway that cause Robinow syndrome, brachydactyly
418 type B and cancer metastasis, and more generally, as a paradigm for modeling genetic
419 disorders.

420

421 **Methods**

422 **Protein expression and purification.** Constructs of human ROR2 (Genbank ID: 19743898)
423 comprising the ECD (residues 34-403), Ig-CRD (60-307), CRD-Kr (171-396) and CRD (171-307)
424 were cloned into the pHLsec vector in frame with a C-terminal His_6-tag (Aricescu et al., 2006).
425 ROR2 constructs were expressed by transient transfection in HEK293T cells with the addition of

426 glycosylation inhibitor kifunensine (Chang et al., 2007). Proteins were isolated from dialyzed
427 conditioned medium via immobilized metal-affinity chromatography and further purified via
428 size exclusion chromatography (SEC) in a buffer containing 10 mM HEPES pH 7.5, 150 mM NaCl.
429
430 **Crystallization and data collection.** Prior to crystallization trials, ROR2 CRD-Kr was concentrated
431 via ultrafiltration to a final concentration of 25 mg mL^{-1} and deglycosylated using catalytic
432 quantities of endoglycosidase F1 (Chang et al., 2007) (0.2 µL/50 µL protein solution). Nanolitre-
433 scale crystallization trials were performed using a Cartesian Technologies robot (100 nL protein
434 plus 100 nL reservoir solution) in 96-well Greiner plates (Walter et al., 2005). ROR2 CRD-Kr
435 crystallized in 0.1 M HEPES pH 7.5, 1.5 M $LiSO_4$ at a temperature of 25 °C. Diffraction data were
436 collected at a temperature of 100 K with crystals mounted within a liquid N_2 cryo-stream.
437 Crystals were treated with 20% (v/v) glycerol supplemented with reservoir solution and flash-
438 cooled in liquid N_2 prior to data collection. For Pt-SAD experiments, ROR2 CRD-Kr crystals were
439 soaked in a saturated solution of K_2PtCl_6 made up in 1 M HEPES pH 7.5, 1.5 M $LiSO_4$ for 1 hour
440 at 25 °C, prior to cryoprotection and harvesting. Data were collected using the rotation method.
441 Diffraction data were scaled and merged using the XIA2 suite and autoPROC (Evans, 2006,
442 Kabsch, 1988, Winter, 2010, Vonrhein et al., 2011).
443
444 **Structure solution.** Initial phases for ROR2 CRD-Kr were obtained using Phenix Autosol with Pt-
445 SAD data (Terwilliger et al., 2009). Four high occupancy Pt sites were identified from
446 substructure solution, and automated model building of the resultant electron density map was
447 performed using the program *Buccaneer* (Cowtan, 2006). This produced an interpretable model

for the CRD (residues 174-307), but phases were not of a high enough quality to properly trace the Kringle domain (residues 308-396). Subsequently, the CRD model generated was utilized as a molecular replacement search model in *Phaser* (McCoy et al., 2007) against higher resolution native data. This solution was fixed and a second search using a homology model for the Kringle domain (generated via Swiss-Model) was performed (Waterhouse et al., 2018). This strategy resulted in higher scores in Phaser (LLG = 424, TFZ = 18.9) than searching for the CRD alone (LLG = 94, TFZ = 9.2), indicative of an improved solution. The model for the ROR2 CRD-Kr was manually built using COOT (Emsley and Cowtan, 2004) and refined to completion using AutoBUSTER (Smart et al., 2012) and Phenix (Terwilliger et al., 2009). Data collection and refinement statistics are shown in Supplementary File 1.

Structure analysis. Stereochemistry was assessed using the MolProbity server (Davis et al., 2007). Superpositions were calculated using *Pymol* (Schrodinger, 2015), which was also used to create ray-traced protein structure images for figures. Residues involved in interactions were identified using both the PDBsum and Pisa servers (Krissinel and Henrick, 2007; Laskowski, 2001). The solvent accessible radius was set to 1.4 Å for the representation of all protein surfaces. Evolutionary structural analysis of CRDs was performed with *SHP* (Riffel et al., 2002; Stuart et al., 1979) and *PHYLIP* (Felsenstein, 1989) to assemble a phylogenetic tree. The structure-based sequence alignment of ROR2 were generated using *UCSF Chimera* (Pettersen et al., 2004) and prepared for presentation using *ALINE* (Okabayashi et al., 1991).

Size Exclusion Chromatography-Multi Angle Light Scattering (SEC-MALS). SEC-MALS experiments were performed using an S200 10/30 column (GE Healthcare) equilibrated in a running buffer of 10 mM HEPES pH 7.5, 150 mM NaCl and coupled to a Wyatt Dawn HELEOS-II MALS detector and Wyatt Optilab rEX refractive index monitor. A 100 µL sample of purified ROR2 ECD was injected at a concentration of 48 µM. ASTRA software (Wyatt Technology) was utilized for data analysis.

Small-angle X-ray scattering (SAXS).

SAXS experiments were carried out on beamline B21, Diamond Light Source, UK at 25°C, over a momentum transfer (q) range of 0.01 $Å^{-1} < q < 0.45$ $Å^{-1}$, where $q = 4\pi \sin(\theta)/\lambda$, and 2θ is the scattering angle. ROR2 CRD-Kr and the ROR2 ECD were injected onto an in-line Shodex KW-402.5 SEC column at concentrations of 6.5 and 8 mg/mL respectively, both in a running buffer of 10 mM Tris pH 7.5, 150 mM NaCl, 1 mM KNO_3. Data were collected with a beam energy of 12.4 keV using a Pilatus P3-2M detector. Data processing and reduction was performed using the program Scatter. Missing residues were added using Modeller (Eswar et al., 2003) and all-atom models generated using Allosmod (Weinkam et al., 2012). A model for the ROR2 Ig domain was generated using the HHpred server (Soding et al., 2005). In each case 50 independent ensembles of 100 models were created. Calculation and fitting of theoretical scattering curves to collected data was performed by FoXS (Schneidman-Duhovny et al., 2010). This procedure was automated via the use of Allosmod-FoXS (Guttman et al., 2013). The best model from Allosmod-FoXS was then used as input for MultiFoXS (Schneidman-Duhovny et al., 2016), for which flexible linker sequences were specified and 10000 independent models

calculated. Sugars were also modelled and simulated via this process. Theoretical SAXS curves were then calculated for each of these models and goodness-of-fit to the experimental data calculated using a chi-square value. Multi-state enumeration was then performed given the chi-square values using the 'branch-and-bound' method, to iteratively find the best multi-state model explaining the data. In the case of ROR2 ECD, MultiFoXS was necessary to find a 2-state model which best explained the data based on flexibility in the linker between the Ig and CRD domains. For the ROR2 CRD-Kr construct, a single-state model calculated using Allosmod-FoXS was sufficient to account for the observed SAXS data.

Mice

The *Ror1*$^{f/f}$*; Ror2*$^{f/f}$*; CAG-CreER* strain was previously described (Ho et al., 2012, Susman et al., 2017, Hayashi and McMahon, 2002) and maintained in a mixed 129 and C57BL/6J background. All animals were used according to the institutional and NIH guidelines approved by the Institutional Animal Care and Use Committee at University of California Davis.

Cell lines

HEK293T (CRL-3216, ATCC, Manassas, VA) cells were initially purchased, re-authenticated by STR profiling (135-XV, ATCC), and tested negative for mycoplasma using the Universal Mycoplasma Detection Kit (30-1012K, ATCC). All cell lines were cultured at 37°C and 5% CO_2 in Dulbecco's Modified Eagles Medium (MT15017CV, Corning) supplemented with 1x glutamine (25-005-CI, Corning), 1x penicillin-streptomycin (30-002-CI, Corning) and 10% fetal bovine serum (16000069, Thermo Fisher Scientific).

513 For derivation of iMEF reporter cells, primary *Ror1*$^{f/f}$; *Ror2*$^{f/f}$; *CAG-CreER* MEFs were
514 isolated directly from E12.5 mouse embryos as described (Susman et al., 2017). Passage 1 or 2
515 cultures were then immortalized by electroporating with Cas9/CRISPR constructs targeting the
516 *Tp53* genes (Addgene Plasmids 88846 and 88847, gifts from Joan Massague (Wang et al., 2017))
517 using the Neon Transfection System (Thermo Fisher). Transformants were serially passaged for
518 3-5 generations until cells from the untransfected control group have died off. For 4-
519 hydroxytamoxifen (H7904, Sigma-Aldrich) treatments, cells were treated with 0.25 µM of 4-
520 hydroxytamoxifen on the first day and then 0.1 µM of 4-hydroxytamoxifen on the subsequent 3
521 days. The 4-hydroxyltamoxifen containing media were replenished daily. To introduce the GFP-
522 Pdzrn3 degradation reporter, a PB (PiggyBac)-GFP-Pdzrn3 plasmid, along with a Super PiggyBac
523 transposase-expressing plasmid, were electroporated into *Ror1*$^{f/f}$; *Ror2*$^{f/f}$; *CAG-CreER* iMEFs and
524 then cultured for 7 days. GFP-positive cells were sorted (MoFlo Astrios Cell Sorter, Beckman
525 Coulter, 488nm laser) to collect the weakly fluorescent (~lowest 1/3 on the FL scale) cells. The
526 iMEF reporter cells were authenticated by STR profiling (137-XV, ATCC), and tested negative for
527 mycoplasma using the Universal Mycoplasma Detection Kit (30-1012K, ATCC).
528
529 **DNA constructs for rescue experiments**
530 The full-length mouse *Ror2* open reading frame (ORF) was amplified from MEF cDNA and
531 subsequently subcloned into a modified pENTR-2B vector carrying the signal sequence from
532 human IgG and the Flag epitope tag upstream of the *Ror2* ORF; the native signal sequence of
533 ROR2 was removed before subcloning. ROR2 truncation mutants and Robinow syndrome
534 mutants were generated by Gibson assembly (Gibson et al., 2009). The following amino acid

535 residues of the mouse ROR2 sequence were deleted in the truncation mutant series: ΔIg, 34-
536 170; ΔCRD, 171-310; ΔKr, 313-402; ΔCRD-Kr, 171-402; ΔICD, 474-944. Mini-ROR2 consists the
537 IgG signal sequence, the Flag tag, CRD-Kr (amino acids 171-402), the monomeric version of the
538 CD45 transmembrane helix (Chin et al., 2005), and the ROR2 juxtamembrane sequence (amino
539 acids 427-473) which contains the epitope for the polyclonal ROR2 antibody used for western
540 detection. ORFs in the pENTR-2B donor vector were then transferred using the Gateway LR
541 Clonase II enzyme mix (11791020, Thermo Fisher) into a modified pLEX_307 lentiviral vector
542 (short EF1 pLEX_307) in which we removed the intron in the EF1 promoter to reduce transgene
543 expression. The original pLEX_307 is a gift from David Root (Plasmid 41392, Addgene). The ORFs
544 in all constructs were verified by Sanger sequencing.
545
546 **Lentiviral protein overexpression**
547 Lentiviruses were packaged and produced in HEK293T cells by co-transfection of the lentiviral
548 vectors with the following packaging plasmids: pRSV-REV, pMD-2-G and pMD-Lg1-pRRE (gifts
549 from Thomas Vierbuchen). 0.1 ml, 0.5 ml or 2.5 ml of the viral supernatants was used to infect
550 *Ror1*$^{f/f}$*; Ror2*$^{f/f}$*; CAG-CreER* iMEFs seeded at 50% confluency in 12-well plates for ~16 hr.
551 Following removal of the virus-containing media, cells were cultured for 24 hr. Infected cells
552 were then split and selected with puromycin (0.0015 mg/ml) for 4-5 days. Cells from the viral
553 titer that killed a large proportion of cells (60–90%) were expanded and used for WNT5A
554 signaling analysis; this ensured that the multiplicity of infection (MOI) is ~1 for all cell lines used
555 in the experiments, with the exception of mini-Ror2. The mini-Ror2 construct is more difficult to

556 express and required a higher titer of virus (2.5 ml), as well as a higher concentration of
557 puromycin (0.002 mg/ml).
558
559 **Antibodies**
560 Antibodies against ROR2 were described previously (Ho et al., 2012, Susman et al., 2017) and
561 used at 1 µg/ml for immunoblotting. The following antibodies were purchased: mouse anti-α-
562 TUBULIN (clone 371 DM1A, ab7291, Abcam); mouse anti-Flag (M2, F1804, Sigma-Aldrich);
563 rabbit anti-WNT5A/B (2530, Cell Signaling Technology); rabbit anti-LRP6 (3395, Cell Signaling
564 Technology); rabbit anti-DVL2 (3216, Cell Signaling Technology); IRDye 800CW goat anti-rabbit
565 IgG (926-32211, Li-Cor); IRDye 800CW goat anti-mouse IgG (926-32210, Li-Cor); IRDye 680RD
566 goat anti-mouse IgG (926-68070, Li-Cor); IRDye 800CW goat anti-mouse IgG (926-32210, Li-
567 Cor). For immunoblotting, commercial primary antibodies were used at 1/1,000 dilution, except
568 for anti-DVL2, which was used at 1/500). Secondary antibodies were used at 1/30,000. The
569 recombinant anti-FZ antibody F2.A was described previously (Pavlovic et al., 2018). The
570 recombinant anti-FZ1 antibody F1.C was generated using phage display methods similar to
571 those described previously (PCT/US2014/051070 and (Pavlovic et al., 2018). Briefly, Fab-phage
572 pools were cycled through 4 rounds of selection for binding to Fc-fused human FZ1 CRD (R&D
573 systems) and clonal phages were screened by ELISA for selectivity for FZ1 CRD over the closely
574 related FZ2 and FZ7 CRDs. Variable domains from FZ1-selective clones were cloned into
575 mammalian expression vectors to enable expression and purification of antibody F1.C in the
576 human IgG1 format, as described (Pavlovic et al., 2018). Isotype control antibodies were
577 generated against the Gaussia luciferase protein.

578

579 **Western blotting**

580 Protein lysates for SDS-PAGE and western blotting were prepared in 1.5x LDS sample buffer
581 (NP0007, Life Technologies). All protein lysates were heated at 95°C for 10 min before SDS-
582 PAGE and western blotting. Quantitative western blotting was performed using the Odyssey
583 DLx (Li-Cor) or Sapphire (Azure BioSystems) infrared scanner according to the manufacturers'
584 instructions. DVL2 phosphorylation was quantified via Image J using the raw images generated
585 from the Odyssey DLx scans.

586

587 **Recombinant proteins and inhibitors**

588 The following recombinant proteins and drug were purchased: human/mouse WNT5A (654-
589 WN-010, R&D Systems); Wnt-C59 (C7641-2s; Cellagen Technology).

590

591 **WNT5A-ROR signaling assays**

592 For flow cytometry-based signaling assay, immortalized MEF cells expressing the GFP-Pdzrn3
593 reporter were plated at a density of 0.02 million/well in 48-well plates three days before
594 WNT5A stimulation. Once adhered to the plate (~1 hr after plating), cells were incubated with
595 Wnt-C59 (100 nM final concentration) and allowed to reach confluency. Wnt-C59 is an inhibitor
596 of the membrane-bound O-acyltransferase Porcupine (Proffitt et al., 2013) and was used in the
597 experiments to block the activity of endogenous WNTs. 72 hr after plating, cells were
598 stimulated with either WNT5A or an equivalent volume of the control buffer (PBS with 0.1%
599 BSA) in the presence of 100 nM Wnt-C59 for 6 hr. Cells were then harvested with trypsin,

600 neutralized with complete culture media, resuspended in PBS + 0.5% FBS and analyzed using a
601 flow cytometer (Cytoflex, Beckman Coulter) (Karuna et al., 2018). Raw data were acquired and
602 analyzed using the CytExpert software (Beckman Coulter). Processing entailed gating out dead
603 cells, calculation of median fluorescence and correction of the GFP-Pdzrn3 reporter signals
604 against the intrinsic autofluorescence of the cells. For anti-FZ whole IgG and Fab treatments
605 without WNT5A, the antibodies were added for 6 hr before flow analysis. For F2.A Fab
606 inhibition of WNT5A-induced signaling, reporter cells were pre-treated with the F2.A Fab for 30
607 min and then stimulated with WNT5A for 6 additional hr; the F2.A Fab was maintained
608 throughout the WNT5A stimulation period.

609 For assaying DVL2 phosphorylation by western blotting, 0.08M cells were seeded per
610 12-well and cultured in the presence of 100nM WNT-C59 until completely confluent (3-4 days).
611 A range of WNT5A concentrations (50-200 ng/ml, or 1.3-5.3 nM) was initially tested. 100 ng/ml
612 (2.6 nM) was found to provide the best dynamic range for DVL2 phosphorylation and was used
613 for all subsequent experiments (shown in Figure 3- figure supplement 2, Figure 4-figure
614 supplement, Figure 5-figure supplement 1).

615

616 **Surface staining of Flag-tagged ROR2**

617 Cells were grown to confluency in 6-well plates and harvested using Accutase (A1110501,
618 Thermo Scientific). The Accutase was neutralized with complete media and then removed by
619 centrifugation. All subsequent steps were performed on ice. Cells were blocked in PBS + 5%
620 goat serum for 20 min, incubated with 0.5 µg/ml anti-Flag antibody diluted in PBS + 5% goat
621 serum for 1 hr. and then washed 3x with PBS. Cells were then incubated with 1 µg/ml Alexa

Fluor 647 goat anti-mouse secondary antibody for 1 hr, washed 3x with PBS, resuspend in PBS + 0.5% FBS and analyzed by flow cytometry. ROR KO cells without rescue and ROR KO cells rescued with WT ROR2 were used as negative and positive controls, respectively.

Endo H and PNGase F sensitivity assay

Protein lysates were collected from cells grown to confluency in 6-well plates using 1X radioimmunoprecipitation (RIPA) buffer (89900, Pierce, Thermo Scientific) supplemented with protease inhibitors (78437, Halt protease inhibitor cocktail, 100X, Thermo Scientific). 120 µg of total protein, in a volume of 60µl was first mixed with glycoprotein denaturation buffer and incubated at 98°C for 10 min. The reaction was then split into three aliquots (36 µg per aliquot in 18 µl) for mock (with no enzyme), Endoglycosidase H (P0704S, New England Biolabs) and peptide N-glycosidase F (P0702S, New England Biolabs) treatments. For enzyme treatments, the 18 µl of denatured lysate was mixed with 2.5 µl of respective reaction buffer and 2.5 µl of enzyme. For PNGase F treatment, 2 µl of NP-40 was added to each reaction. The reaction volume was brought up to 25 µl for all reactions and incubated at 37°C for 2 hr. The samples were analyzed by western blotting for LRP6, ROR2 and α-TUBULIN.

WNT5A-CRD binding assay

DNA fragments encoding the ROR2 CRD (residues 170-311), FZ2 CRD (40-165) and FZ7 CRD (45-170) were subcloned into a modified pCX-Fc vector to express CRD fusion proteins that are N-terminally fused to the signal sequence of human IgG and the Flag tag and C-terminally fused to the Fc fragment of human IgG. The native signal sequence of ROR2, FZ2 and FZ7 were removed

644 during subcloning. As a negative control in the WNT5A binding, a construct containing the
645 signal sequence of human IgG, the Flag tag and the Fc fragment, but no CRD, was generated. All
646 constructs were confirmed by Sanger sequencing. The resulting constructs were transiently
647 transfected into HEK293T cells and cultured in DMEM supplemented with 10% fetal bovine
648 serum, glutamine and penicillin/streptomycin. 16 hr after transfection, culture media were
649 replaced with DMEM supplemented with 10% KnockOut serum replacement (10828010;
650 Thermo Scientific), glutamine and penicillin/streptomycin, and conditioned for 24 hr. KnockOut
651 serum replacement was used to avoid the IgG in fetal bovine serum from being carried over
652 into the subsequent Fc fusion-Protein A bead binding reactions. After collection, the
653 conditioned media, which were quite acidic based on their yellowish appearance, were
654 neutralized with 20 µl of 1.5 M Tris pH 8.8 and centrifuged to remove cell debris. A pilot binding
655 experiment was performed using Protein A Plus UltraLink beads (53142; Thermo Scientific) to
656 determine the relative expression of the Fc proteins. This information was used to normalize
657 the volume of each conditioned media to be used in the final WNT5A binding experiment such
658 that the molar ratio of each Fc fusion protein on the beads is approximately equal. For the
659 WNT5A pulldown experiment, normalized volumes of conditioned media were incubated with
660 25 µl packed volume of Protein A-Sepharose beads at 4°C for 16 hr with rotation. The beads
661 were washed 3x with cold PBS and then incubated with 540 ng of purified recombinant WNT5A
662 per Fc construct in 1.5 ml of PBS + 5 mg/ml BSA. The binding reactions were incubated at 4°C
663 for 16 hr, after which the beads were washed 3x with cold PBS. Proteins bound to the beads
664 were eluted by heating at 95°C for 10 min in 2x Laemmli buffer supplemented with β-
665 mercaptoethanol and analyzed by western blotting. To minimize potential cross-reactivity of

the secondary antibody toward the Fc portion of the fusion proteins on western blots, the goat anti-rabbit IRDye 800CW antibody used in the experiment was pre-absorbed against Fc immobilized on a nitrocellulose membrane. The anti-WNT5A antibody shows some cross-reactivity to ROR2 CRD, which explains the higher molecular weight (~65kD) band seen in the uncropped blot of Figure 4A.

Acknowledgements

We thank members of the Siebold and Ho labs for their input and discussions. We thank the staff of Diamond Light Source UK beamlines I03, I23 and B21 for assistance (MX14744 and MX19946), and K. El Omari, T. Walter, K. Harlos and D. Staunton for technical support. We thank Michael Greenberg and Linda Hu (Harvard Medical School) for providing anti-ROR2 antibodies. We thank Gen Wen Lim, Claudia Wang, Morgan Krueger, Ember Hung and Vaishanavi Sware for experimental assistance; Bridget McLaughlin and Jonathan Van Dyke at the UC Davis Cancer Center Flow Cytometry core for training and technical assistance (supported by National Cancer Institute 2P30CA093373-19 and S10 OD018223). This work was supported by the National Institutes of Health (1R35GM119574, 1R35GM144341) to H.H.H., and Cancer Research UK (C20724/A26752 and DRCRPG-May23/100002) to C.S. S.C.G. was supported by a Wellcome Trust-funded DPhil studentship (099675/Z/12/Z). Additional support from the Wellcome Trust Core Award Grant Number 203141/Z/16/Z is acknowledged.

References

AFZAL, A. R., RAJAB, A., FENSKE, C. D., OLDRIDGE, M., ELANKO, N., TERNES-PEREIRA, E., TUYSUZ, B., MURDAY, V. A., PATTON, M. A., WILKIE, A. O. & JEFFERY, S. 2000. Recessive Robinow

syndrome, allelic to dominant brachydactyly type B, is caused by mutation of ROR2. *Nat Genet,* 25**,** 419-22.

ARTIM, S. C., MENDROLA, J. M. & LEMMON, M. A. 2012. Assessing the range of kinase autoinhibition mechanisms in the insulin receptor family. *Biochem J,* 448**,** 213-20.

BAZAN, J. F. & DE SAUVAGE, F. J. 2009. Structural ties between cholesterol transport and morphogen signaling. *Cell,* 138**,** 1055-6.

BUNN, K. J., DANIEL, P., ROSKEN, H. S., O'NEILL, A. C., CAMERON-CHRISTIE, S. R., MORGAN, T., BRUNNER, H. G., LAI, A., KUNST, H. P., MARKIE, D. M. & ROBERTSON, S. P. 2015. Mutations in DVL1 cause an osteosclerotic form of Robinow syndrome. *Am J Hum Genet,* 96**,** 623-30.

BYRNE, E. F. X., SIRCAR, R., MILLER, P. S., HEDGER, G., LUCHETTI, G., NACHTERGAELE, S., TULLY, M. D., MYDOCK-MCGRANE, L., COVEY, D. F., RAMBO, R. P., SANSOM, M. S. P., NEWSTEAD, S., ROHATGI, R. & SIEBOLD, C. 2016. Structural basis of Smoothened regulation by its extracellular domains. *Nature,* 535**,** 517-522.

CARRON, C., PASCAL, A., DJIANE, A., BOUCAUT, J. C., SHI, D. L. & UMBHAUER, M. 2003. Frizzled receptor dimerization is sufficient to activate the Wnt/beta-catenin pathway. *J Cell Sci,* 116**,** 2541-50.

CHIN, C. N., SACHS, J. N. & ENGELMAN, D. M. 2005. Transmembrane homodimerization of receptor-like protein tyrosine phosphatases. *FEBS Lett,* 579**,** 3855-8.

DANN, C. E., HSIEH, J. C., RATTNER, A., SHARMA, D., NATHANS, J. & LEAHY, D. J. 2001. Insights into Wnt binding and signalling from the structures of two Frizzled cysteine-rich domains. *Nature,* 412**,** 86-90.

DEBRUINE, Z. J., KE, J., HARIKUMAR, K. G., GU, X., BOROWSKY, P., WILLIAMS, B. O., XU, W., MILLER, L. J., XU, H. E. & MELCHER, K. 2017. Wnt5a promotes Frizzled-4 signalosome assembly by stabilizing cysteine-rich domain dimerization. *Genes Dev,* 31**,** 916-926.

DECHIARA, T. M., KIMBLE, R. B., POUEYMIROU, W. T., ROJAS, J., MASIAKOWSKI, P., VALENZUELA, D. M. & YANCOPOULOS, G. D. 2000. Ror2, encoding a receptor-like tyrosine kinase, is required for cartilage and growth plate development. *Nat Genet,* 24**,** 271-4.

DEGUCHI, H., TAKEYA, H., GABAZZA, E. C., NISHIOKA, J. & SUZUKI, K. 1997. Prothrombin kringle 1 domain interacts with factor Va during the assembly of prothrombinase complex. *Biochem J,* 321 (Pt 3)**,** 729-35.

DIRAC, A. M. & BERNARDS, R. 2003. Reversal of senescence in mouse fibroblasts through lentiviral suppression of p53. *J Biol Chem,* 278**,** 11731-4.

ESWAR, N., JOHN, B., MIRKOVIC, N., FISER, A., ILYIN, V. A., PIEPER, U., STUART, A. C., MARTI-RENOM, M. A., MADHUSUDHAN, M. S., YERKOVICH, B. & SALI, A. 2003. Tools for comparative protein structure modeling and analysis. *Nucleic Acids Res,* 31**,** 3375-80.

EVANS, P. 2006. Scaling and assessment of data quality. *Acta Crystallogr D Biol Crystallogr,* 62**,** 72-82.

GIBSON, D. G., YOUNG, L., CHUANG, R. Y., VENTER, J. C., HUTCHISON, C. A., 3RD & SMITH, H. O. 2009. Enzymatic assembly of DNA molecules up to several hundred kilobases. *Nat Methods,* 6**,** 343-5.

GOYDEL, R. S., WEBER, J., PENG, H., QI, J., SODEN, J., FREETH, J., PARK, H. & RADER, C. 2020. Affinity maturation, humanization, and co-crystallization of a rabbit anti-human ROR2 monoclonal antibody for therapeutic applications. *J Biol Chem,* 295**,** 5995-6006.

GREEN, J. L., KUNTZ, S. G. & STERNBERG, P. W. 2008. Ror receptor tyrosine kinases: orphans no more. *Trends Cell Biol,* 18**,** 536-44.

GRUMOLATO, L., LIU, G., MONG, P., MUDBHARY, R., BISWAS, R., ARROYAVE, R., VIJAYAKUMAR, S., ECONOMIDES, A. N. & AARONSON, S. A. 2010. Canonical and noncanonical Wnts use a common mechanism to activate completely unrelated coreceptors. *Genes Dev,* 24**,** 2517-30.

GUARINO, S. R., DI BELLO, A., PALAMINI, M., CAPILLO, M. C. & FORNERIS, F. 2022. Crystal structure of the kringle domain of human receptor tyrosine kinase-like orphan receptor 1 (hROR1). *Acta Crystallogr F Struct Biol Commun,* 78**,** 185-192.

GUTTMAN, M., WEINKAM, P., SALI, A. & LEE, K. K. 2013. All-atom ensemble modeling to analyze small-angle x-ray scattering of glycosylated proteins. *Structure,* 21**,** 321-31.

HAYASHI, S. & MCMAHON, A. P. 2002. Efficient recombination in diverse tissues by a tamoxifen-inducible form of Cre: a tool for temporally regulated gene activation/inactivation in the mouse. *Dev Biol,* 244**,** 305-18.

HO, H. Y., SUSMAN, M. W., BIKOFF, J. B., RYU, Y. K., JONAS, A. M., HU, L., KURUVILLA, R. & GREENBERG, M. E. 2012. Wnt5a-Ror-Dishevelled signaling constitutes a core developmental pathway that controls tissue morphogenesis. *Proc Natl Acad Sci U S A,* 109**,** 4044-51.

JANDA, C. Y. & GARCIA, K. C. 2015. Wnt acylation and its functional implication in Wnt signalling regulation. *Biochem Soc Trans,* 43**,** 211-6.

JANDA, C. Y., WAGHRAY, D., LEVIN, A. M., THOMAS, C. & GARCIA, K. C. 2012. Structural basis of Wnt recognition by Frizzled. *Science,* 337**,** 59-64.

KABSCH, W. 1988. Automatic indexing of rotation diffraction patterns. *J. Appl. Cryst.,* 21**,** 67-72.

KARUNA, E. P., SUSMAN, M. W. & HO, H. H. 2018. Quantitative Live-cell Reporter Assay for Noncanonical Wnt Activity. *Bio Protoc,* 8.

KIM, C. & FORRESTER, W. C. 2003. Functional analysis of the domains of the C elegans Ror receptor tyrosine kinase CAM-1. *Dev Biol,* 264**,** 376-90.

KIPPS, T. J. 2022. ROR1: an orphan becomes apparent. *Blood,* 140**,** 1583-1591.

KONOPELSKI, S. E., SUSMAN MW, KUNZ R, TAN J, COHEN MD, OKADA K, LAMB H, CHOI SC, KARUNA EP, SCALES MK, GYGI SP, GREENBERG ME, HO HH. 2021. Proteomic analysis identifies the E3 ubiquitin ligase Pdzrn3 as a regulatory target of Wnt5a-Ror signaling. *Proc Natl Acad Sci U S A,* 118**,** e2104944118.

KONOPELSKI SNAVELY, S. E., SRINIVASAN, S., DREYER, C. A., TAN, J., CARRAWAY, K. L., 3RD & HO, H. H. 2023. Non-canonical WNT5A-ROR signaling: New perspectives on an ancient developmental pathway. *Curr Top Dev Biol,* 153**,** 195-227.

MEHAWEJ, C., CHOUERY, E., MAALOUF, D., BAUJAT, G., LE MERRER, M., CORMIER-DAIRE, V. & MEGARBANE, A. 2012. Identification of a novel causative mutation in the ROR2 gene in a Lebanese family with a mild form of recessive Robinow syndrome. *Eur J Med Genet,* 55**,** 103-8.

MIKELS, A. J. & NUSSE, R. 2006. Purified Wnt5a protein activates or inhibits beta-catenin-TCF signaling depending on receptor context. *PLoS Biol,* 4**,** e115.

MINAMI, Y., OISHI, I., ENDO, M. & NISHITA, M. 2010. Ror-family receptor tyrosine kinases in noncanonical Wnt signaling: their implications in developmental morphogenesis and human diseases. *Dev Dyn,* 239**,** 1-15.

MOON, R. T., CAMPBELL, R. M., CHRISTIAN, J. L., MCGREW, L. L., SHIH, J. & FRASER, S. 1993. Xwnt-5A: a maternal Wnt that affects morphogenetic movements after overexpression in embryos of Xenopus laevis. *Development,* 119**,** 97-111.

NACHTERGAELE, S., WHALEN, D. M., MYDOCK, L. K., ZHAO, Z., MALINAUSKAS, T., KRISHNAN, K., INGHAM, P. W., COVEY, D. F., SIEBOLD, C. & ROHATGI, R. 2013. Structure and function of the Smoothened extracellular domain in vertebrate Hedgehog signaling. *Elife,* 2**,** e01340.

NAGASAKI, K., NISHIMURA, G., KIKUCHI, T., NYUZUKI, H., SASAKI, S., OGAWA, Y. & SAITOH, A. 2018. Nonsense mutations in FZD2 cause autosomal-dominant omodysplasia: Robinow syndrome-like phenotypes. *Am J Med Genet A,* 176**,** 739-742.

NILE, A. H., MUKUND, S., STANGER, K., WANG, W. & HANNOUSH, R. N. 2017. Unsaturated fatty acyl recognition by Frizzled receptors mediates dimerization upon Wnt ligand binding. *Proc Natl Acad Sci U S A,* 114**,** 4147-4152.

OISHI, I., SUZUKI, H., ONISHI, N., TAKADA, R., KANI, S., OHKAWARA, B., KOSHIDA, I., SUZUKI, K., YAMADA, G., SCHWABE, G. C., MUNDLOS, S., SHIBUYA, H., TAKADA, S. & MINAMI, Y. 2003. The receptor tyrosine kinase Ror2 is involved in non-canonical Wnt5a/JNK signalling pathway. *Genes Cells,* 8**,** 645-54.

OKABAYASHI, K., NAKAGAWA, Y., HAYASUKE, N., OHI, H., MIURA, M., ISHIDA, Y., SHIMIZU, M., MURAKAMI, K., HIRABAYASHI, K., MINAMINO, H. & ET AL. 1991. Secretory expression of the human serum albumin gene in the yeast, Saccharomyces cerevisiae. *J Biochem,* 110**,** 103-10.

OLDRIDGE, M., FORTUNA, A. M., MARINGA, M., PROPPING, P., MANSOUR, S., POLLITT, C., DECHIARA, T. M., KIMBLE, R. B., VALENZUELA, D. M., YANCOPOULOS, G. D. & WILKIE, A. O. 2000. Dominant mutations in ROR2, encoding an orphan receptor tyrosine kinase, cause brachydactyly type B. *Nat Genet,* 24**,** 275-8.

PAVLOVIC, Z., ADAMS, J. J., BLAZER, L. L., GAKHAL, A. K., JARVIK, N., STEINHART, Z., ROBITAILLE, M., MASCALL, K., PAN, J., ANGERS, S., MOFFAT, J. & SIDHU, S. S. 2018. A synthetic anti-Frizzled antibody engineered for broadened specificity exhibits enhanced anti-tumor properties. *MAbs,* 10**,** 1157-1167.

PERSON, A. D., BEIRAGHI, S., SIEBEN, C. M., HERMANSON, S., NEUMANN, A. N., ROBU, M. E., SCHLEIFFARTH, J. R., BILLINGTON, C. J., JR., VAN BOKHOVEN, H., HOOGEBOOM, J. M., MAZZEU, J. F., PETRYK, A., SCHIMMENTI, L. A., BRUNNER, H. G., EKKER, S. C. & LOHR, J. L. 2010. WNT5A mutations in patients with autosomal dominant Robinow syndrome. *Dev Dyn,* 239**,** 327-37.

PROFFITT, K. D., MADAN, B., KE, Z., PENDHARKAR, V., DING, L., LEE, M. A., HANNOUSH, R. N. & VIRSHUP, D. M. 2013. Pharmacological inhibition of the Wnt acyltransferase PORCN prevents growth of WNT-driven mammary cancer. *Cancer Res,* 73**,** 502-7.

REBAGAY, G., YAN, S., LIU, C. & CHEUNG, N. K. 2012. ROR1 and ROR2 in Human Malignancies: Potentials for Targeted Therapy. *Front Oncol,* 2**,** 34.

SALDANHA, J., SINGH, J. & MAHADEVAN, D. 1998. Identification of a Frizzled-like cysteine rich domain in the extracellular region of developmental receptor tyrosine kinases. *Protein Sci,* 7**,** 1632-5.

SATO, A., YAMAMOTO, H., SAKANE, H., KOYAMA, H. & KIKUCHI, A. 2010. Wnt5a regulates distinct signalling pathways by binding to Frizzled2. *EMBO J,* 29**,** 41-54.

SCHNEIDMAN-DUHOVNY, D., HAMMEL, M. & SALI, A. 2010. FoXS: a web server for rapid computation and fitting of SAXS profiles. *Nucleic Acids Res,* 38**,** W540-4.

SCHNEIDMAN-DUHOVNY, D., HAMMEL, M., TAINER, J. A. & SALI, A. 2016. FoXS, FoXSDock and MultiFoXS: Single-state and multi-state structural modeling of proteins and their complexes based on SAXS profiles. *Nucleic Acids Res,* 44**,** W424-9.

SCHWABE, G. C., TINSCHERT, S., BUSCHOW, C., MEINECKE, P., WOLFF, G., GILLESSEN-KAESBACH, G., OLDRIDGE, M., WILKIE, A. O., KOMEC, R. & MUNDLOS, S. 2000. Distinct mutations in the receptor tyrosine kinase gene ROR2 cause brachydactyly type B. *Am J Hum Genet,* 67**,** 822-31.

SHEN, G., KE, J., WANG, Z., CHENG, Z., GU, X., WEI, Y., MELCHER, K., XU, H. E. & XU, W. 2015. Structural basis of the Norrin-Frizzled 4 interaction. *Cell Res,* 25**,** 1078-81.

SHI, F., MENDROLA, J. M., SHEETZ, J. B., WU, N., SOMMER, A., SPEER, K. F., NOORDERMEER, J. N., KAN, Z. Y., PERRY, K., ENGLANDER, S. W., STAYROOK, S. E., FRADKIN, L. G. & LEMMON, M. A. 2021. ROR and RYK extracellular region structures suggest that receptor tyrosine kinases have distinct WNT-recognition modes. *Cell Rep,* 37**,** 109834.

SODING, J., BIEGERT, A. & LUPAS, A. N. 2005. The HHpred interactive server for protein homology detection and structure prediction. *Nucleic Acids Res,* 33**,** W244-8.

STIEGLER, A. L., BURDEN, S. J. & HUBBARD, S. R. 2009. Crystal structure of the frizzled-like cysteine-rich domain of the receptor tyrosine kinase MuSK. *J Mol Biol,* 393**,** 1-9.

SUSMAN, M. W., KARUNA, E. P., KUNZ, R. C., GUJRAL, T. S., CANTU, A. V., CHOI, S. S., JONG, B. Y., OKADA, K., SCALES, M. K., HUM, J., HU, L. S., KIRSCHNER, M. W., NISHINAKAMURA, R., YAMADA, S., LAIRD, D. J., JAO, L. E., GYGI, S. P., GREENBERG, M. E. & HO, H. H. 2017. Kinesin superfamily protein Kif26b links Wnt5a-Ror signaling to the control of cell and tissue behaviors in vertebrates. *Elife,* 6.

TAMHANKAR, P. M., VASUDEVAN, L., KONDURKAR, S., YASHASWINI, K., AGARWALLA, S. K., NAIR, M., RAMKUMAR, T. V., CHAUBAL, N. & CHENNURI, V. S. 2014. Identification of novel ROR2 gene mutations in Indian children with Robinow syndrome. *J Clin Res Pediatr Endocrinol,* 6**,** 79-83.

TERWILLIGER, T. C., ADAMS, P. D., READ, R. J., MCCOY, A. J., MORIARTY, N. W., GROSSE-KUNSTLEVE, R. W., AFONINE, P. V., ZWART, P. H. & HUNG, L. W. 2009. Decision-making in structure solution using Bayesian estimates of map quality: the PHENIX AutoSol wizard. *Acta Crystallogr D Biol Crystallogr,* 65**,** 582-601.

TUFAN, F., CEFLE, K., TURKMEN, S., TURKMEN, A., ZORBA, U., DURSUN, M., OZTURK, S., PALANDUZ, S., ECDER, T., MUNDLOS, S. & HORN, D. 2005. Clinical and molecular characterization of two adults with autosomal recessive Robinow syndrome. *Am J Med Genet A,* 136**,** 185-9.

ULTSCH, M., LOKKER, N. A., GODOWSKI, P. J. & DE VOS, A. M. 1998. Crystal structure of the NK1 fragment of human hepatocyte growth factor at 2.0 A resolution. *Structure,* 6**,** 1383-93.

VAN BOKHOVEN, H., CELLI, J., KAYSERILI, H., VAN BEUSEKOM, E., BALCI, S., BRUSSEL, W., SKOVBY, F., KERR, B., PERCIN, E. F., AKARSU, N. & BRUNNER, H. G. 2000. Mutation of the gene encoding the ROR2 tyrosine kinase causes autosomal recessive Robinow syndrome. *Nat Genet,* 25**,** 423-6.

VEEMAN, M. T., AXELROD, J. D. & MOON, R. T. 2003. A second canon. Functions and mechanisms of beta-catenin-independent Wnt signaling. *Dev Cell,* 5**,** 367-77.

VONRHEIN, C., FLENSBURG, C., KELLER, P., SHARFF, A., SMART, O., PACIOREK, W., WOMACK, T. & BRICOGNE, G. 2011. Data processing and analysis with the autoPROC toolbox. *Acta Crystallogr D Biol Crystallogr,* 67**,** 293-302.

WANG, Q., ZOU, Y., NOWOTSCHIN, S., KIM, S. Y., LI, Q. V., SOH, C. L., SU, J., ZHANG, C., SHU, W., XI, Q., HUANGFU, D., HADJANTONAKIS, A. K. & MASSAGUE, J. 2017. The p53 Family Coordinates Wnt and Nodal Inputs in Mesendodermal Differentiation of Embryonic Stem Cells. *Cell Stem Cell,* 20**,** 70-86.

WATERHOUSE, A., BERTONI, M., BIENERT, S., STUDER, G., TAURIELLO, G., GUMIENNY, R., HEER, F. T., DE BEER, T. A. P., REMPFER, C., BORDOLI, L., LEPORE, R. & SCHWEDE, T. 2018. SWISS-MODEL: homology modelling of protein structures and complexes. *Nucleic Acids Res,* 46**,** W296-W303.

WEINKAM, P., PONS, J. & SALI, A. 2012. Structure-based model of allostery predicts coupling between distant sites. *Proc Natl Acad Sci U S A,* 109**,** 4875-80.

WHITE, J., MAZZEU, J. F., HOISCHEN, A., JHANGIANI, S. N., GAMBIN, T., ALCINO, M. C., PENNEY, S., SARAIVA, J. M., HOVE, H., SKOVBY, F., KAYSERILI, H., ESTRELLA, E., VULTO-VAN SILFHOUT, A. T., STEEHOUWER, M., MUZNY, D. M., SUTTON, V. R., GIBBS, R. A., BAYLOR-HOPKINS CENTER FOR MENDELIAN, G., LUPSKI, J. R., BRUNNER, H. G., VAN BON, B. W. & CARVALHO, C. M. 2015. DVL1 frameshift mutations clustering in the penultimate exon cause autosomal-dominant Robinow syndrome. *Am J Hum Genet,* 96**,** 612-22.

WHITE, J. J., MAZZEU, J. F., COBAN-AKDEMIR, Z., BAYRAM, Y., BAHRAMBEIGI, V., HOISCHEN, A., VAN BON, B. W. M., GEZDIRICI, A., GULEC, E. Y., RAMOND, F., TOURAINE, R., THEVENON, J., SHINAWI, M., BEAVER, E., HEELEY, J., HOOVER-FONG, J., DURMAZ, C. D., KARABULUT, H. G., MARZIOGLU-OZDEMIR, E., CAYIR, A., DUZ, M. B., SEVEN, M., PRICE, S., FERREIRA, B. M., VIANNA-MORGANTE, A. M., ELLARD, S., PARRISH, A., STALS, K., FLORES-DABOUB, J., JHANGIANI, S. N., GIBBS, R. A., BAYLOR-HOPKINS CENTER FOR MENDELIAN, G., BRUNNER, H. G., SUTTON, V. R., LUPSKI, J. R. & CARVALHO, C. M. B. 2018. WNT Signaling Perturbations Underlie the Genetic Heterogeneity of Robinow Syndrome. *Am J Hum Genet,* 102**,** 27-43.

WHITE, J. J., MAZZEU, J. F., HOISCHEN, A., BAYRAM, Y., WITHERS, M., GEZDIRICI, A., KIMONIS, V., STEEHOUWER, M., JHANGIANI, S. N., MUZNY, D. M., GIBBS, R. A., BAYLOR-HOPKINS CENTER FOR MENDELIAN, G., VAN BON, B. W. M., SUTTON, V. R., LUPSKI, J. R., BRUNNER, H. G. & CARVALHO, C. M. B. 2016. DVL3 Alleles Resulting in a -1 Frameshift of the Last Exon Mediate Autosomal-Dominant Robinow Syndrome. *Am J Hum Genet,* 98**,** 553-561.

WINTER, G. 2010. xia2: an expert system for macromolecular crystallography data reduction. *J. Appl. Cryst.,* 43**,** 186-190.

XU, Y. K. & NUSSE, R. 1998. The Frizzled CRD domain is conserved in diverse proteins including several receptor tyrosine kinases. *Curr Biol,* 8**,** R405-6.

YU, H., YE, X., GUO, N. & NATHANS, J. 2012. Frizzled 2 and frizzled 7 function redundantly in convergent extension and closure of the ventricular septum and palate: evidence for a network of interacting genes. *Development,* 139**,** 4383-94.
ZEBISCH, M., JACKSON, V. A., ZHAO, Y. & JONES, E. Y. 2016. Structure of the Dual-Mode Wnt Regulator Kremen1 and Insight into Ternary Complex Formation with LRP6 and Dickkopf. *Structure,* 24**,** 1599-605.

Figure Legends

Figure 1. Structure of the ROR2 CRD and Kringle domains. **A)** Domain layout of ROR2 and constructs used in this study. **B)** Cartoon representation of the ROR2 CRD-Kr structural unit coloured in a rainbow representation (N terminus: blue, C terminus: red), with secondary structural elements indicated and disulfide bonds numbered using Roman numerals. The right panel shows a 2-domain representation of ROR2, with the CRD in salmon and the Kringle domain in blue. **C)** Close-up view on the ROR2 CRD-Kr interface rotated 90° relative to **B**. Interface residues are shown in stick representation and colour-coded as in B, right panel. Hydrogen bonds are displayed as a dashed line. **D)** Structural phylogenetic analysis of CRDs, adapted from Figure 5 of (Nachtergaele et al., 2013) to include ROR2.

Figure 1-figure supplement 1. ROR2 purification, characterization and structure solution. **A)** Western blot analysis of the secretion of soluble ROR2 constructs from HEK293T cells. Deletion of the Kr domain impairs secretion. **B)** SEC-MALS analysis of the ROR2 ECD at 2 mg mL^{-1} (48 µM). The ROR2 ECD elutes as a monomeric species with a molecular weight of 45.4 kDa, as displayed by the red line. **C)** Purity assessment by SDS-PAGE of ROR2 ECD construct purified via IMAC and SEC. **D)** Identification of sulfur sites in ROR2 CRD-Kr using long-wavelength data

929 collection at I23. A total of 8 disulfide bonds (I-VII) could be resolved, as well as 4 methionine
930 and 1 cysteine side chains, as well as 2 sulfate ions. **E-H)** Structure solution of ROR2 CRD-Kr
931 using MR-SAD. The final structure refined using *PHENIX* and corresponding sigma-A weighted
932 $2F_o$-map at 1σ (blue) and F_o-F_c density at +/- 3.5σ (green/red) are shown. Panel E focuses on the
933 ROR2 CRD-Kr interface, whereas panels F-H are centred around the palmitoleate binding site
934 commonly conserved in Fz-type CRDs. This site is occluded in the ROR2 structure by a
935 rearrangement of a loop (M212-T219) that overlaps with palmitoleate binding, observed, for
936 example, in the Fz8-xWNT8 complex structure (PDB ID: 4F0A) (Janda et al., 2012). The
937 superposition of ROR2 and the Fz8xWNT8 complex (G and H) illustrates this rearrangement.
938
939 **Figure 1-figure supplement 2. Comparison of the ROR2 Kr to other related Kr structures. A)**
940 Structural superposition of the ROR2 CRD-Kr (salmon) with described human ROR1 Kr (yellow,
941 PDB 7TNG), human ROR2 Kr (green, PDB 6OSN) and Drosophila Nrk (grey, PDB 7ME4). Cα
942 RMSDs shown are with respect to ROR2 Kr within the CRD-Kr structure. **B)** Sequence alignment
943 of the human ROR2 and Drosophila Nrk CRD-Kr tandem domains. **(C)** Comparison of the human
944 ROR2 and Drosophila Nrk CRD-Kr tandem domains shown as ribbon representation. The CRDs
945 of ROR2 and Nrk are shown in the same spatial orientation.
946
947 **Figure 2. Comparison of the ROR2 CRD to other FZ-type CRDs**. **A-D)** CRDs are shown as surface
948 representation and coloured according to hydrophobicity (green: hydrophobic to white:
949 hydrophilic). Displayed structures: **A)** FZ8-PAM (palmitoleate) complex (PDB 4F0A) (Janda et al.,
950 2012), **B)** FZ8-apo (PDB 1IJY) (Dann et al., 2001), **C)** Smoothened-CLR (cholesterol) complex (PDB

5L7D) (Byrne et al., 2016) and **D)** ROR2 (from this study). **E)** Structure-based sequence alignment of the ROR2 and FZ8 CRDs. The ROR2 inserted helix α5 is shown with a dashed box. (**F**) Structural superposition of the ROR2 CRD (salmon) with the FZ8-WNT8 (green/purple, PDB 4F0A) complex. Only the WNT8 'lipid thumb' is shown, with the covalently attached palmitoleate modification in white.

Figure 2-figure supplement 1. SAXS solution structure of the ROR2 ECD. A) Experimental scattering curve (black) and calculated scattering from models (blue), shown to a maximum momentum transfer of 0.35 $Å^{-1}$. A fitting residual between the experimental and calculated scattering patterns is displayed. **B)** The ROR2 ECD data is best explained using two major models in the given populations as calculated by Multi-FOXS, indicating flexibility in the linker between the Ig and the CRD-Kr regions. **C)** Experimental (black) and calculated (blue) Guinier region. The shaded area indicates the region used for R_g analysis. The calculated radius of gyration (R_g) and molecular weight derived from the volume of correlation metric V_c (MW_{VC}) are displayed. **D)** Normalised pair distance distribution (P(r)) function and derived maximum intra-particle distance distribution function (D_{max}).

Figure 2-figure supplement 2. Comparison of the human ROR2 and Drosophila Nrk CRDs. Structural superposition of the human ROR2 CRD (salmon) with the Drosophila Nrk CRD (purple, PDB 7ME4). The Cα RMSD between the two structures is shown. The close-up view shows the region surrounding the internally buried fatty acid in the Drosophila Nrk CRD.

973 **Figure 3. Requirement of the ROR2 CRD in WNT5A signaling**

974 **A)** Workflow of the ROR2 central rescue paradigm. Primary MEFs generated from E12.5 *ROR1$^{f/f}$;*
975 *ROR2$^{f/f}$; CAG-CreER* conditional knockout (ROR cKO) mouse embryos were immortalized by
976 CRISPR/Cas9-mediated deletion of the *Tp53* gene. A WNT5A-ROR signaling reporter (GFP-
977 Pdzrn3) was stably inserted in the immortalized MEFs (iMEFs) via piggyBac-based transposition.
978 ROR cKO iMEFs were then treated with 4-hydroxytamoxifen (4OHT) to activate the CreER
979 recombinase to delete the *Ror1* and *Ror2* genes, resulting in ROR knockout (ROR KO) iMEFs
980 (genotype: *ROR1$^{-/-}$; ROR2$^{-/-}$; CAG-CreER*). To compare the function of ROR2 domain truncation
981 mutants, WT or mutant ROR2 rescue constructs were re-expressed in ROR KO iMEFs via
982 lentiviral transduction. **B)** Western blot showing expression of endogenous ROR2 in ROR cKO
983 iMEFs, the loss of ROR2 expression in ROR KO iMEFs, and re-expression of the WT ROR2 rescue
984 construct (Flag-tagged). **C)** Dose-response curves showing WNT5A-ROR signaling activity,
985 assayed by GFP-Pdzrn3 degradation, as a function of WNT5A concentration in ROR cKO iMEFs,
986 ROR KO iMEFs or ROR KO iMEFs expressing the WT ROR2 rescue construct. All iMEFs were
987 pretreated with Wnt-C59, an inhibitor of the membrane-bound O-acyltransferase Porcupine
988 (Proffitt et al., 2013), to block the activity of endogenous WNTs. Each datapoint was calculated
989 from the median fluorescence ([after WNT5A stimulation – before WNT5A stimulation]/before
990 WNT5A stimulation) of the GFP-Pdzrn3 reporter from 10,000 cells. Error bars represent ± SEM
991 calculated from two technical replicates (two independent WNT5A stimulation experiments of
992 the same cell lines). **D)** Schematic of ROR2 domain truncation mutants. **E)** Western blot showing
993 expression of the WT and mutant ROR2 constructs. ROR2 protein variants were detected using
994 a rabbit polyclonal anti-ROR2 antibody. α-TUBULIN was used as the loading control. **F)**

995 Quantification of the effects of ROR2 mutant variants in rescuing WNT5A-ROR signaling, as
996 assayed by GFP-Pdzrn3 degradation. Cells were treated with 200 ng/ml (5.3 nM) WNT5A for 6
997 hr. Error bars represent ± SEM calculated from three technical replicates. t-test (unpaired) was
998 performed to determine statistical significance of each rescue construct vs. the no rescue
999 control (ROR KO cells). **G)** Schematic of the mini-ROR2 construct. **H)** Anti-ROR2 western blot
1000 showing expression of the WT ROR2 and mini-ROR2 rescue constructs. α-TUBULIN was used as
1001 the loading control. **I)** Quantification of the effect of mini-ROR2 in rescuing WNT5A-ROR
1002 signaling, as assayed by GFP-Pdzrn3 degradation. Cells were treated with 200 ng/ml (5.3 nM)
1003 WNT5A for 6 hr. Error bars represent ± SEM calculated from three technical replicates. t-test
1004 (unpaired) was performed to determine statistical significance of each rescue construct vs. the
1005 no rescue control (ROR KO cells). Figure 3 – source data 1 (related to panel C). Figure 3 – source
1006 data 2 (related to panel F). Figure 3 – source data 3 (related to panel I).
1007
1008 **Figure 3-figure supplement 1. Surface expression analysis of ROR2 domain truncation**
1009 **mutants and mini-ROR2**. WT and ROR2 domain truncation mutants were tagged on the N-
1010 terminus with a Flag tag (see Materials and Methods for details). Anti-Flag immunostaining was
1011 performed on live cells to assess the cell surface expression levels of ROR2 domain truncation
1012 mutants **(A)**, and mini-ROR2 **(B)**. ROR KO cells and ROR KO cells expressing the WT ROR2 rescue
1013 construct were used as the negative and positive controls, respectively.
1014
1015 **Figure 3-figure supplement 2. Requirement of the ROR2 CRD in WNT5A signaling as assayed**
1016 **by DVL2 phosphorylation**. **(A)** Western blots showing the extents of DVL2 phosphorylation in

ROR KO iMEFs and in ROR KO iMEFs expressing WT or domain truncation mutants of ROR2, before and after WNT5A stimulation (100 ng/ml or 2.6 nM WNT5A for 6 hr). DVL2 phosphorylation causes a delay in the gel mobility DVL2 in SDS-PAGE, which can be visualized as an upward shift of the DVL2 band (marked as P-DVL2). **(B)** Quantification of DVL2 phosphorylation by densitometry. % phosphorylation is calculated as the portion of total DVL2 signal that is upshifted. **(C)** Western blots showing the extents of DVL2 phosphorylation in ROR KO iMEFs and in ROR KO iMEFs expressing WT ROR2 or mini-ROR2, before and after WNT5A stimulation (100 ng/ml or 2.6 nM WNT5A for 6hr). **(D)** Quantification of DVL2 phosphorylation by densitometry. % phosphorylation is calculated as the portion of total DVL2 signal that is upshifted.

Figure 4. Involvement of FZ in WNT5A-ROR signaling

A) Fc fusions of the ROR2, FZ2 and FZ7 CRDs immobilized on protein A-coated beads were tested for their ability to pull down WNT5A. Protein A beads alone and protein A beads coated with Fc were used as negative controls. 9.3% of the input and 33% of the pulled down materials were analyzed on a 12% SDS-polyacrylamide gel. WNT5A and Fc fusion proteins were detected by western blotting using anti-WNT5A and anti-Flag antibodies (all Fc fusions were tagged with the Flag epitope), respectively. **B)** Quantification of the effects of the pan-anti-FZ IgG F2.A and anti-FZ1 IgG F1.C in inducing GFP-Pdzrn3 reporter degradation in ROR cKO iMEFs, ROR KO iMEFs and ROR KO iMEFs rescued with WT ROR2. WNT5A was used as the positive control, and an isotype-matching IgG against the Gaussia luciferase was used as the negative control (Ctrl IgG). No IgGs and WNT5A were mixed in this experiment. All IgGs were used at 200 nM, and

1039 WNT5A was used at 200 ng/ml (5.3 nM). WNT5A and FZ IgG stimulations were done in the
1040 presence of Wnt-C59 for 6 hr. Each data point was calculated from the median fluorescence
1041 ([after antibody treatment – before antibody treatment]/before antibody treatment) of the
1042 GFP-Pdzrn3 reporter. Error bars represent ± SEM calculated from three technical replicates;
1043 20,000 cells per replicate. t-test (unpaired) was performed to determine the statistical
1044 significance of each treatment vs. PBS. **C)** Dose-response analysis showing the ability of the
1045 bivalent pan-anti-FZ IgG F2.A to activate WNT5A signaling, as assayed by GFP-Pdzrn3
1046 degradation in ROR KO iMEFs treated with Wnt-C59 but without WNT5A. **D)** Dose-response
1047 analysis showing the ability of the bivalent anti-FZ1 IgG F1.C to activate WNT5A signaling, as
1048 assayed by GFP-Pdzrn3 degradation in ROR KO iMEFs treated with Wnt-C59 but without
1049 WNT5A. **E)** Quantification of the effects of the monovalent Fab fragment of the F2.A antibody in
1050 inducing GFP-Pdzrn3 degradation in ROR cKO iMEFs, ROR KO iMEFs and ROR KO iMEFs rescued
1051 with WT ROR2. All iMEFs were treated with Wnt-C59. WNT5A was used as the positive control,
1052 and an isotype-matching Fab against the Gaussia luciferase was used at the negative control
1053 (Ctrl Fab). The Ctrl and F2.A Fabs were used at 200 nM, and WNT5A was used at 200 ng/ml (5.3
1054 nM). No cells were simultaneously treated with Fab and WNT5A in this experiment. Each data
1055 point was calculated from the median fluorescence ([after antibody treatment – before
1056 antibody treatment]/before antibody treatment) of the GFP-Pdzrn3 reporter. Error bars
1057 represent ± SEM calculated from three technical replicates; 20,000 cells per replicate. t-test
1058 (unpaired) was performed to determine statistical significance of each treatment vs. PBS. **F)**
1059 Quantification of the effects of the monovalent Fab fragment of the F2.A antibody in inhibiting
1060 WNT5A-induced GFP-Pdzrn3 reporter degradation in ROR cKO iMEFs, ROR KO iMEFs and ROR

1061 KO iMEFs rescued with WT ROR2. All iMEFs were treated with Wnt-C59. An isotype-matching
1062 Fab against the Gaussia luciferase was used at the negative control (Ctrl Fab). In all conditions,
1063 cells were pre-treated with PBS, Ctrl Fab or F2.A Fab for 30 min and then stimulating with
1064 WNT5A in the presence of the PBS or Fabs for an additional 6 hr. The Ctrl and F2.A Fabs were
1065 used at 200 nM, and WNT5A was used at 200 ug/ml (5.3 nM). Each data point was calculated
1066 from the median fluorescence ([after WNT5A treatment – before WNT5A treatment]/before
1067 WNT5A treatment) of the GFP-Pdzrn3 reporter. Error bars represent ± SEM calculated from
1068 three technical replicates; 20,000 cells per replicate. t-test (unpaired) was performed to
1069 determine statistical significance of each treatment vs. PBS. Figure 4 – source data 1 (related to
1070 panel B). Figure 4 – source data 2 (related to panel C). Figure 4 – source data 3 (related to panel
1071 D). Figure 4 – source data 4 (related to panel E). Figure 4- source data 5 (related to panel F).
1072
1073 **Figure 4-figure supplement. Activation of WNT5A signaling by anti-FZ IgGs, as assayed by**
1074 **DVL2 phosphorylation**. **(A)** Western blots showing the abilities of F1.C and F2.A IgG to activate
1075 WNT5A signaling, as assayed by DVL2 phosphorylation, in ROR cKO iMEFs, ROR KO MEFs, and
1076 ROR KO iMEFs rescued with WT ROR2. The Ctrl, F2.A and F1.C IgGs were used at 200 nM, and
1077 WNT5A was used at 100 ng/ml (2.6 nM). Cells were pretreated with Wnt-C59 and maintained in
1078 Wnt-C59 during the 6-hr stimulation period. **(B)** Quantification of DVL2 phosphorylation by
1079 densitometry. % phosphorylation is calculated as the portion of total DVL2 signal that is
1080 upshifted.
1081
1082 **Figure 5. Analysis of Robinow syndrome mutations in the ROR2 CRD and Kr domains**

1083 **A)** Western blot showing expression of WT ROR2 and Robinow syndrome ROR2 mutants in the
1084 ROR KO iMEF reporter cells. **B)** Quantification of the effects of Robinow syndrome ROR2
1085 mutants in rescuing WNT5A-ROR signaling, as assayed by GFP-Pdzrn3 degradation. Cells were
1086 treated with 200 ng/ml (5.26 nM) WNT5A for 6 hr. Error bars represent ± SEM calculated from
1087 three technical replicates. t-test (unpaired) was performed to determine statistical significance
1088 for mutants vs. WT ROR2 rescue. **C)** Western blots showing the sensitivity of WT ROR2 and
1089 Robinow syndrome ROR2 mutants to Endo H and PNGase F. LRP6 was used as a control
1090 substrate for Endo H and PNGase F, and α-TUBULIN was used as the loading control. **D)**
1091 Structure of the ROR2 CRD-Kr tandem domains showing the location of the Robinow syndrome
1092 mutations. **E)** Close-up view of C223 and R272. **F)** Close-up view of C182, R184 and R189. **G)**
1093 Close-up view of G326 and R366. Figure 5 – source data 1 (related to panel B).
1094
1095 **Figure 5-figure supplement 1. Signaling capabilities of Robinow syndrome mutants, as**
1096 **assayed by DVL2 phosphorylation**. **(A)** Western blots showing the abilities of WT ROR2 and
1097 Robinow syndrome ROR2 mutants to rescue WNT5A signaling in the ROR KO iMEF reporter
1098 cells, as assayed by DVL2 phosphorylation. Wnt-C59 pretreated cells were stimulated with
1099 WNT5A (100 ng/ml or 2.6 nM) for 6hr. **(B)** Quantification of DVL2 phosphorylation by
1100 densitometry. % phosphorylation is calculated as the portion of total DVL2 signal that is
1101 upshifted.
1102
1103 **Figure 5-figure supplement 2. Surface expression analysis of Robinow syndrome mutations in**
1104 **the ROR2 CRD and Kr domains**. WT ROR2 and Robinow syndrome ROR2 mutants were tagged

on the N-terminus with a Flag tag. Anti-Flag immunostaining was performed on live cells to assess the cell surface expression levels of these ROR2 mutants. ROR KO cells and ROR KO cells expressing the WT ROR2 rescue construct were used as the negative and positive controls, respectively.

Figure 6. Model of ROR2 CRD and FZ action in WNT5A-ROR signaling.

See text for details.

Supplementary File 1. Data collection and refinement statistics for ROR2 CRD-Kr

Data in parenthesis refer to highest resolution shell unless otherwise stated. RMSD: Root Mean Square Deviation.

Supplementary File 2. Evolutionary analysis of CRD structures.

[A]PDB accession codes displayed in parenthesis; [B]RMSD values were calculated for equivalent Cα atom positions using the program SHP (Riffel et al., 2002; Stuart et al., 1979); [C]Number of equivalent Cα positions used in calculation of RMSD values with SHP; [D]Summed structural correlation (total probability) values calculated via SHP. The phylogenetic tree for CRDs analyzed (Figure 1C) was assembled using PHYLIP (Felsenstein, 1989). These summed structural correlation values were used to construct a distance matrix. Fz8-PAM – Frizzled 8-palmitoleate complex (Janda et al., 2012), Smo – Smoothened (Byrne et al., 2016), Fz8 – Frizzled 8 (Dann et al., 2001), sFRP3 – secreted Frizzled-related protein 3 (Dann et al., 2001), MuSK – muscle-specific kinase (Stiegler et al., 2009), NPC1 – Niemann-Pick C1 protein (Kwon et al., 2009), RFBP

– riboflavin-binding protein (Monaco, 1997), FRα – folate receptor α (Chen et al., 2013), FRβ – folate receptor β (Wibowo et al., 2013), JUNO – folate receptor δ (Han et al., 2016). Fz7 – Frizzled 7 (Nile et al., 2017).

Titles for source data linked to figures:

Figure 3-source data 1. (Related to panel C). Dose-response curves showing WNT5A-ROR signaling activity, as assayed by GFP-Pdzrn3 degradation.

Figure 3-source data 2. (Related to panel F). Quantification of the effects of ROR2 mutant variants in rescuing WNT5A-ROR signaling, as assayed by GFP-Pdzrn3 degradation.

Figure 3-source data 3. (Related to panel I). Quantification of the effect of mini-ROR2 in rescuing WNT5A-ROR signaling, as assayed by GFP-Pdzrn3 degradation.

Figure 4-source data 1. (Related to panel B). Quantification of the effects of the anti-pan FZ IgG F2.A and anti-FZ1 IgG F1.C in inducing GFP-Pdzrn3 reporter degradation.

Figure 4-source data 2. (Related to panel C). Dose-response analysis showing the ability of the bivalent anti-pan FZ IgG F2.A to activate WNT5A signaling, as assayed by GFP-Pdzrn3 degradation.

Figure 4-source data 3. (Related to panel D). Dose-response analysis showing the ability of the bivalent anti-FZ1 IgG F1.C to activate WNT5A signaling, as assayed by GFP-Pdzrn3 degradation.

Figure 4-source data 4. (Related to panel E). Quantification of the effects of the monovalent Fab fragment of the F2.A antibody in inducing GFP-Pdzrn3 reporter degradation.

Figure 4-source data 5. (Related to panel F). Quantification of the effects of the monovalent Fab fragment of the F2.A antibody in inhibiting WNT5A-induced GFP-Pdzrn3 reporter degradation.

Figure 5-source data 1. (Related to panel B). Quantification of the effects of Robinow syndrome ROR2 mutants in rescuing WNT5A-ROR signaling, as assayed by GFP-Pdzrn3 degradation.

Figure 1

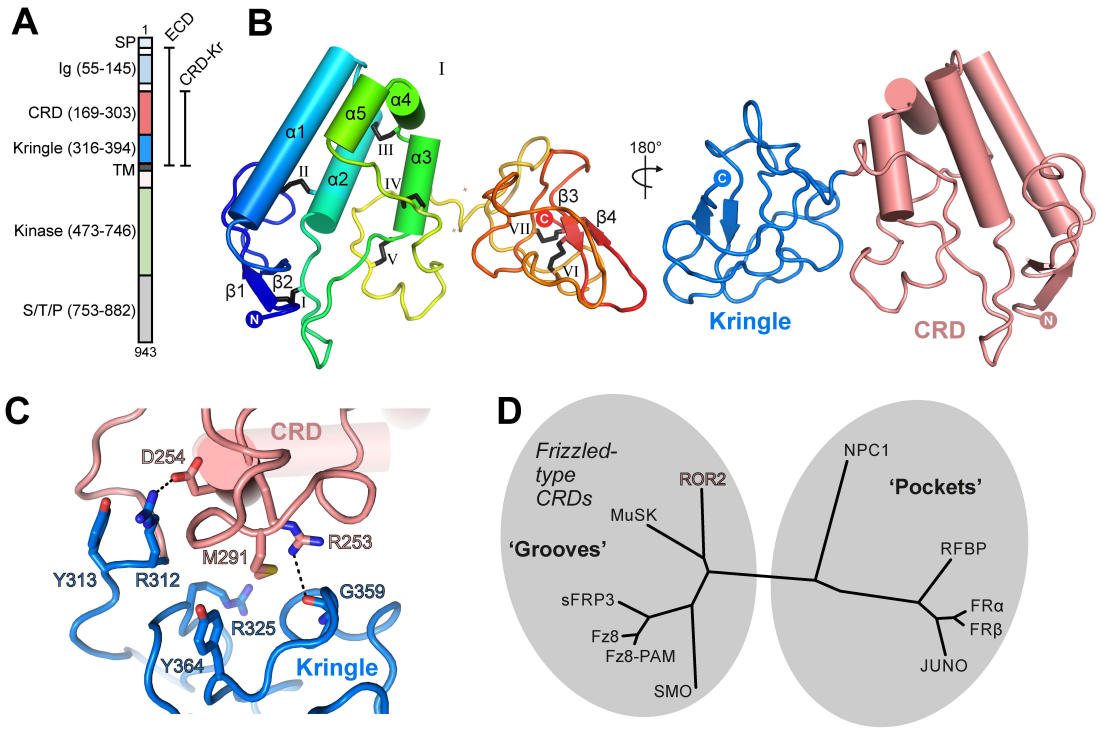
A
SP
1
ECD
CRD-Kr
Ig (55-145)
CRD (169-303)
Kringle (316-394)
TM
Kinase (473-746)
S/T/P (753-882)
943
B
α1
α2
α3
α4
α5
β1
β2
β3
β4
I
II
III
IV
V
VI
VII
N
180°
Kringle
CRD
C
CRD
D254
R253
M291
Y313
R312
G359
R325
Y364
Kringle
D
Frizzled-type CRDs
'Grooves'
ROR2
MuSK
sFRP3
Fz8
Fz8-PAM
SMO
NPC1
'Pockets'
RFBP
FRα
FRβ
JUNO

Figure 1-figure supplement 1

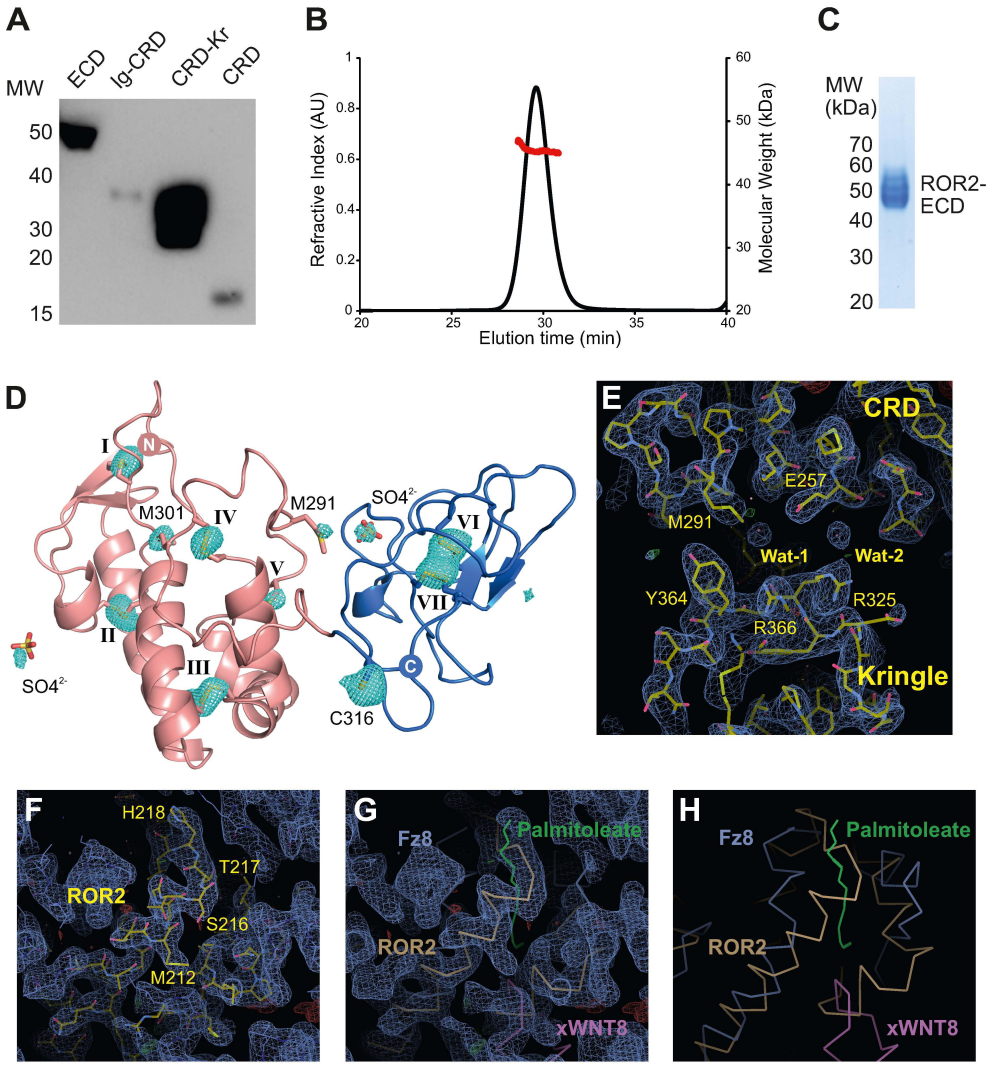

Figure 1-figure supplement 2

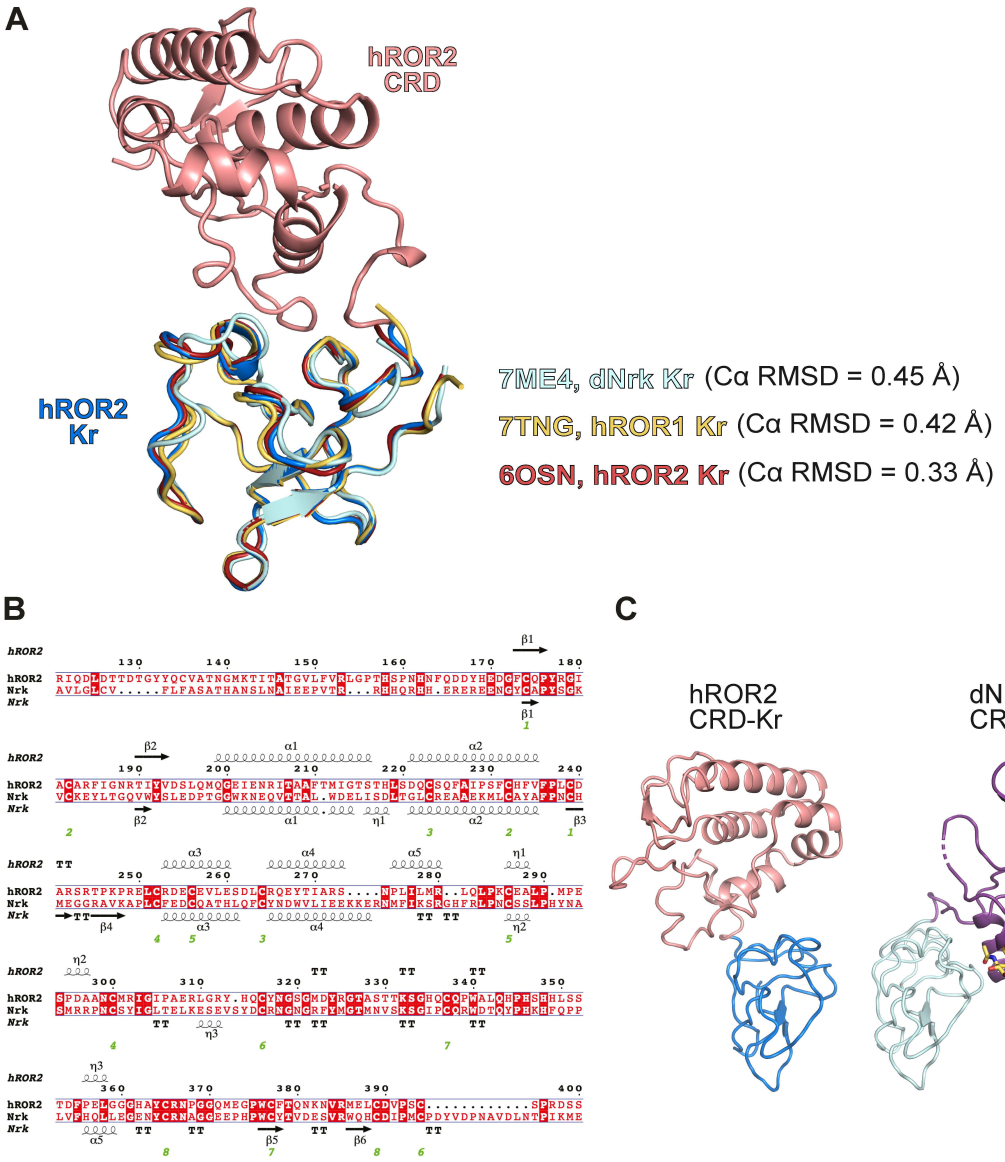

Figure 2

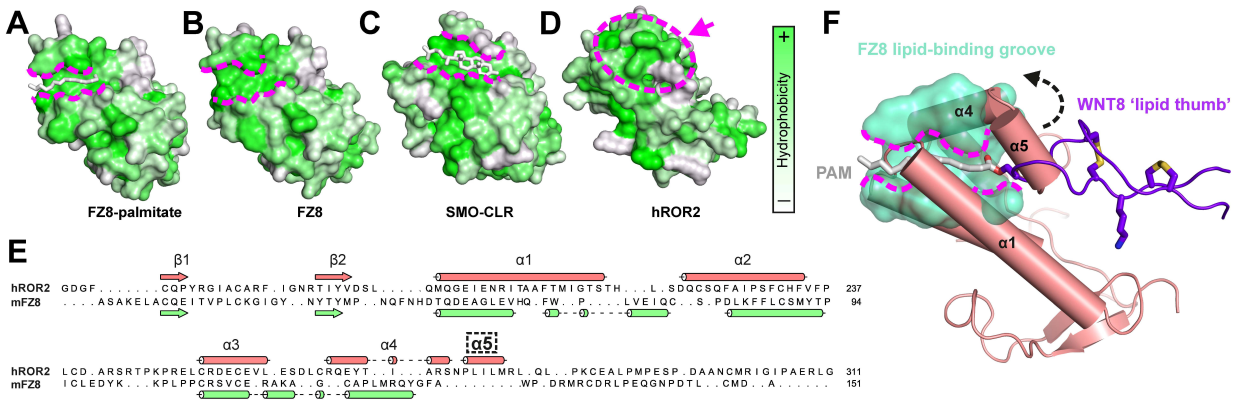
A
B
C
D
F
FZ8-palmitate
FZ8
SMO-CLR
hROR2
Hydrophobicity
+
–
FZ8 lipid-binding groove
WNT8 'lipid thumb'
α4
α5
α1
PAM

E
β1
β2
α1
α2
hROR2 GDGF.....CQPYRGIACARF.IGNRTIYVDSL.....QMQGEIENRITAAFTMIGTSTH...L.SDQCSQFAIPSFCHFVFP 237
mFZ8 ....ASAKELACQEITVPLCKGIGY..NYTYMP..NQFNHDTQDEAGLEVHQ.FW..P....LVEIQC..S.PDLKFFLCSMYTP 94
α3
α4
α5
hROR2 LCD.ARSRTPKPRELCRDECEVL.ESDLCRQEYT..I...ARSNPLILMRL.QL..PKCEALPMPESP.DAANCMRIGIPAERLG 311
mFZ8 ICLEDYK...KPLPPCRSVCE.RAKA..G..CAPLMRQYGFA.....WP.DRMRCDRLPEQGNPDTL..CMD..A..... 151

Figure 2-figure supplement 1

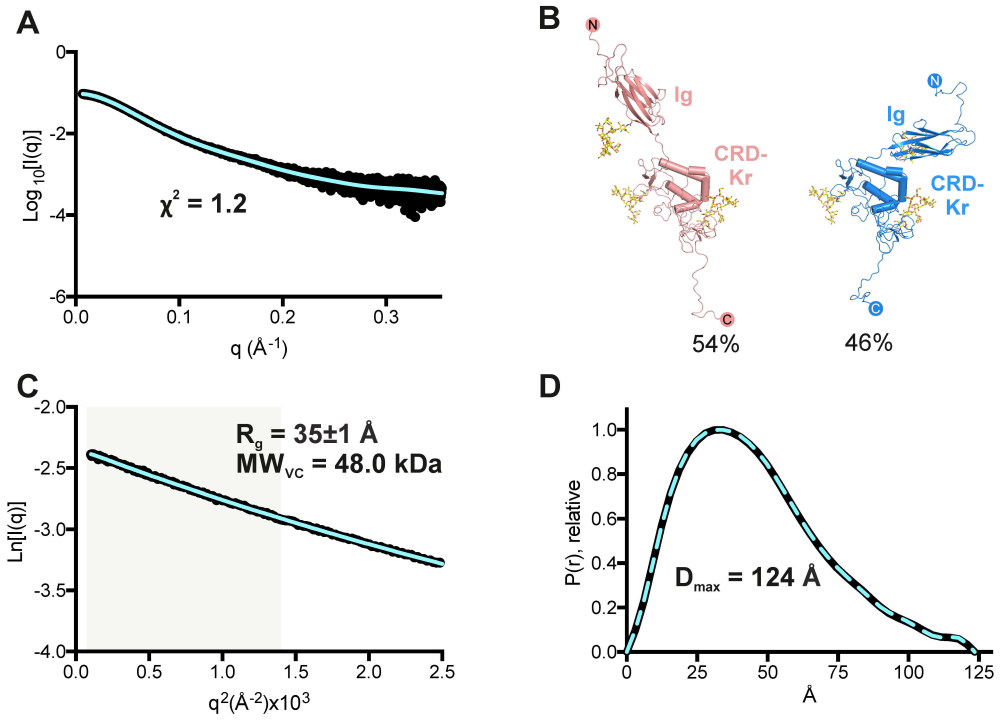

Figure 2-figure supplement 2

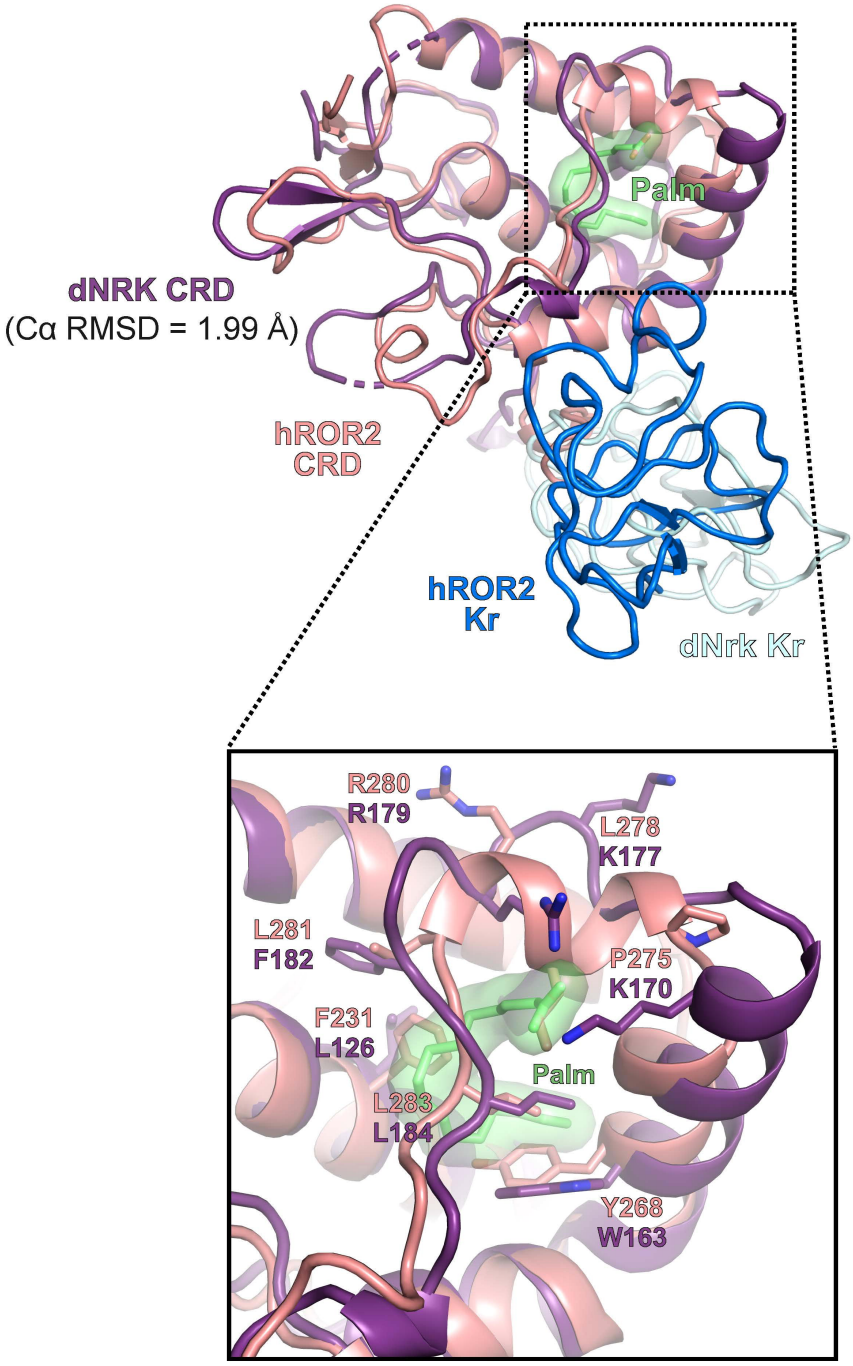

Figure 3

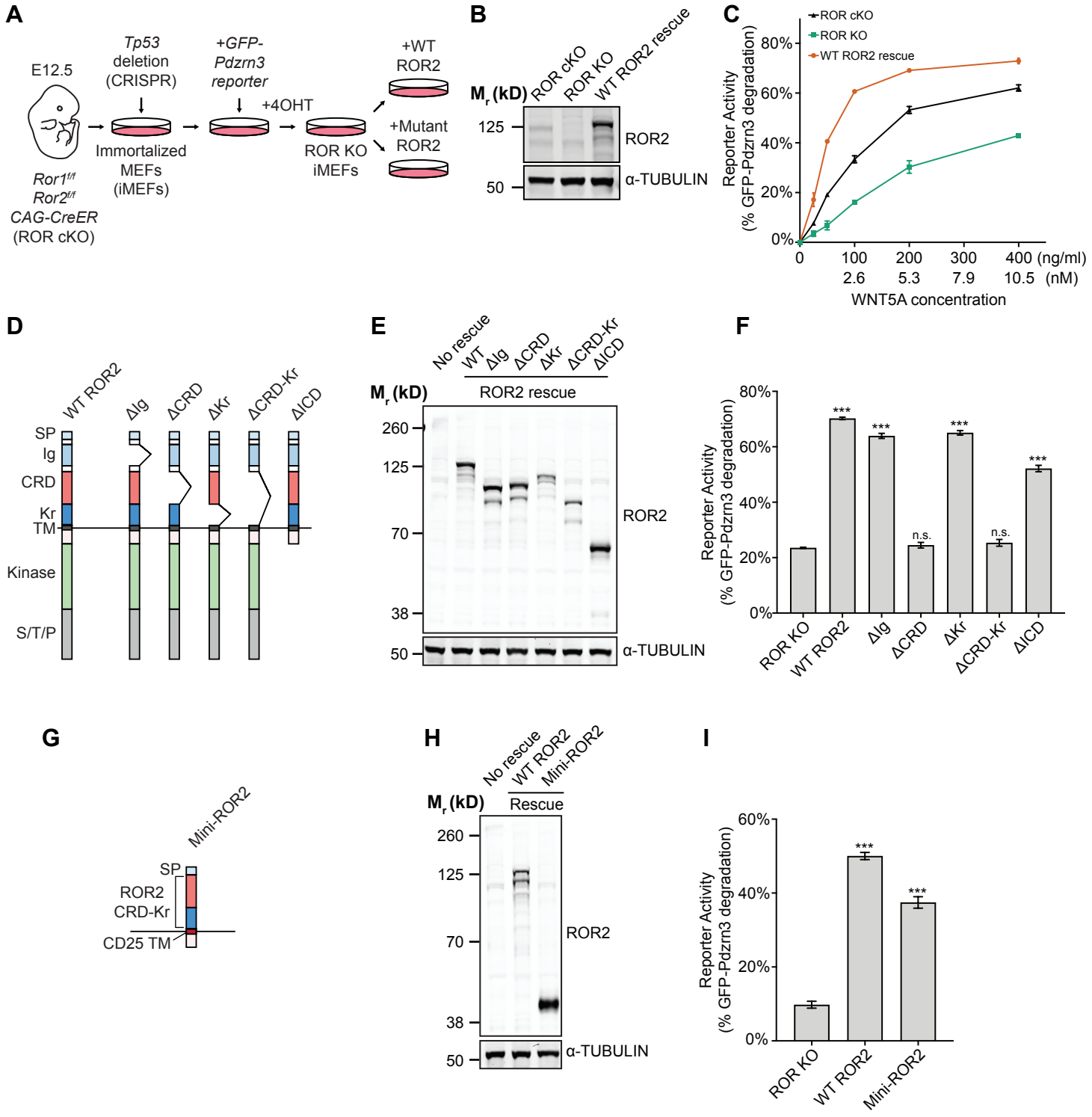
A
E12.5
Ror1f/f
Ror2f/f
CAG-CreER
(ROR cKO)
Tp53
deletion
(CRISPR)
Immortalized
MEFs
(iMEFs)
+GFP-
Pdzrn3
reporter
+4OHT
ROR KO
iMEFs
+WT
ROR2
+Mutant
ROR2
B
Mr (kD)
ROR cKO
ROR KO
WT ROR2 rescue
125
50
ROR2
α-TUBULIN
C
ROR cKO
ROR KO
WT ROR2 rescue
Reporter Activity
(% GFP-Pdzrn3 degradation)
80%
60%
40%
20%
0%
0
100
200
300
400 (ng/ml)
2.6
5.3
7.9
10.5 (nM)
WNT5A concentration
D
WT ROR2
ΔIg
ΔCRD
ΔKr
ΔCRD-Kr
ΔICD
SP
Ig
CRD
Kr
TM
Kinase
S/T/P
E
No rescue
WT
ΔIg
ΔCRD
ΔKr
ΔCRD-Kr
ΔICD
ROR2 rescue
Mr (kD)
260
125
70
38
50
ROR2
α-TUBULIN
F
Reporter Activity
(% GFP-Pdzrn3 degradation)
80%
60%
40%
20%
0%
***
n.s.
ROR KO
WT ROR2
ΔIg
ΔCRD
ΔKr
ΔCRD-Kr
ΔICD
G
Mini-ROR2
SP
ROR2
CRD-Kr
CD25 TM
H
No rescue
WT ROR2
Mini-ROR2
Rescue
Mr (kD)
260
125
70
38
50
ROR2
α-TUBULIN
I
Reporter Activity
(% GFP-Pdzrn3 degradation)
60%
40%
20%
0%
***
ROR KO
WT ROR2
Mini-ROR2

Figure 3-figure supplement 1

A

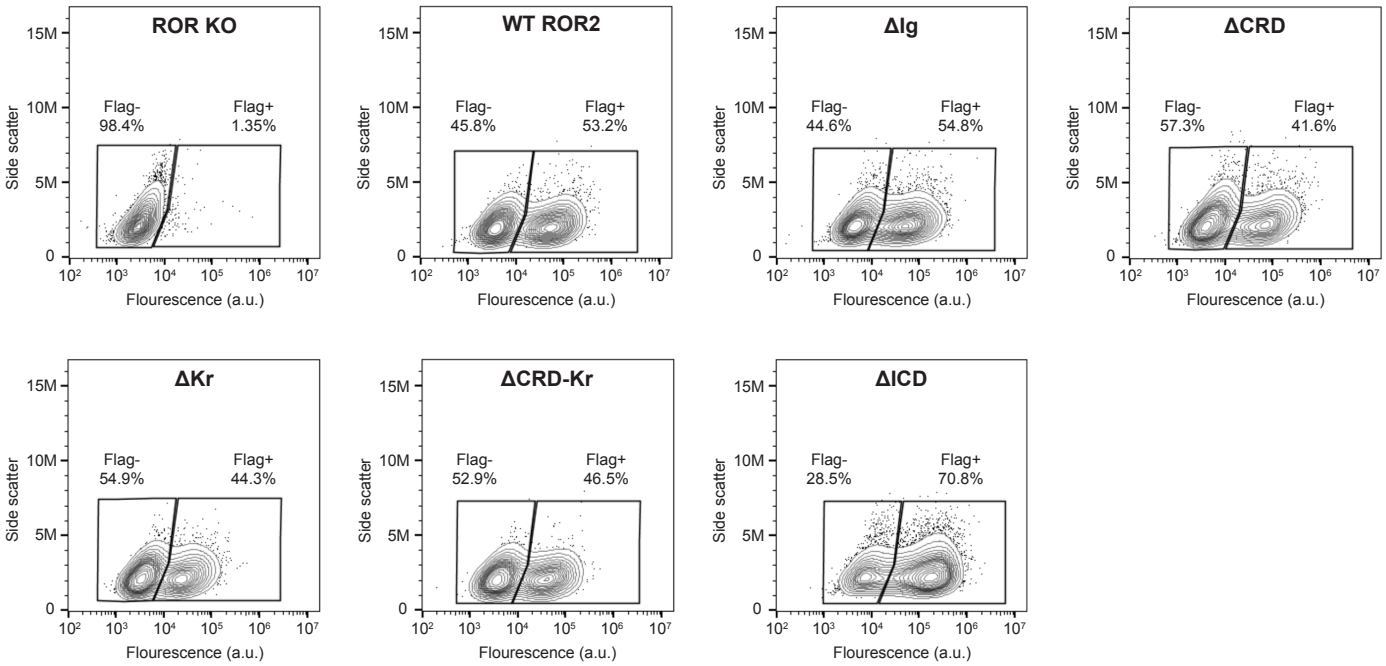

B

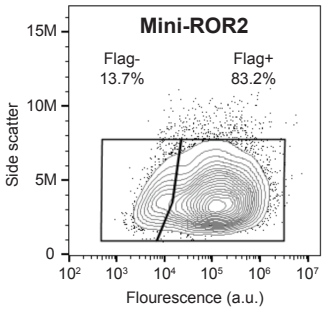

Figure 3-figure supplement 2

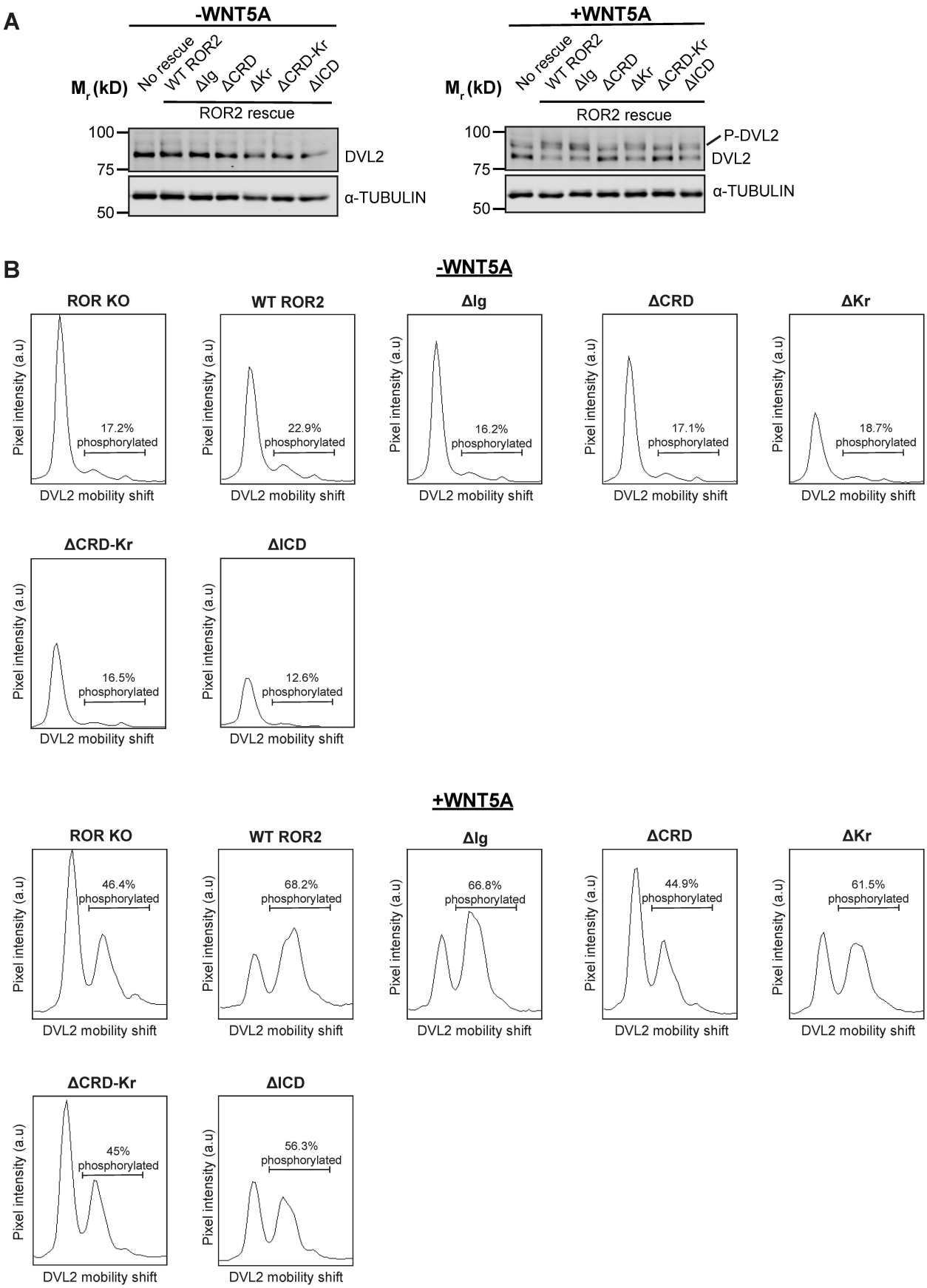

Figure 3-figure supplement 2

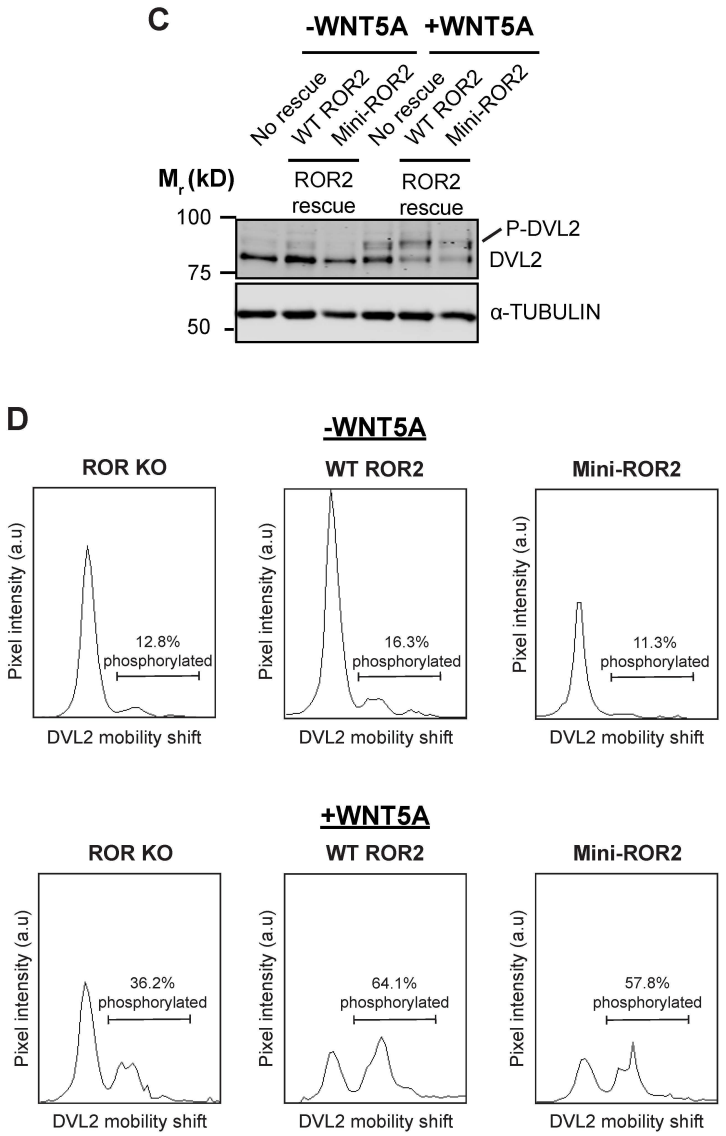

Figure 4

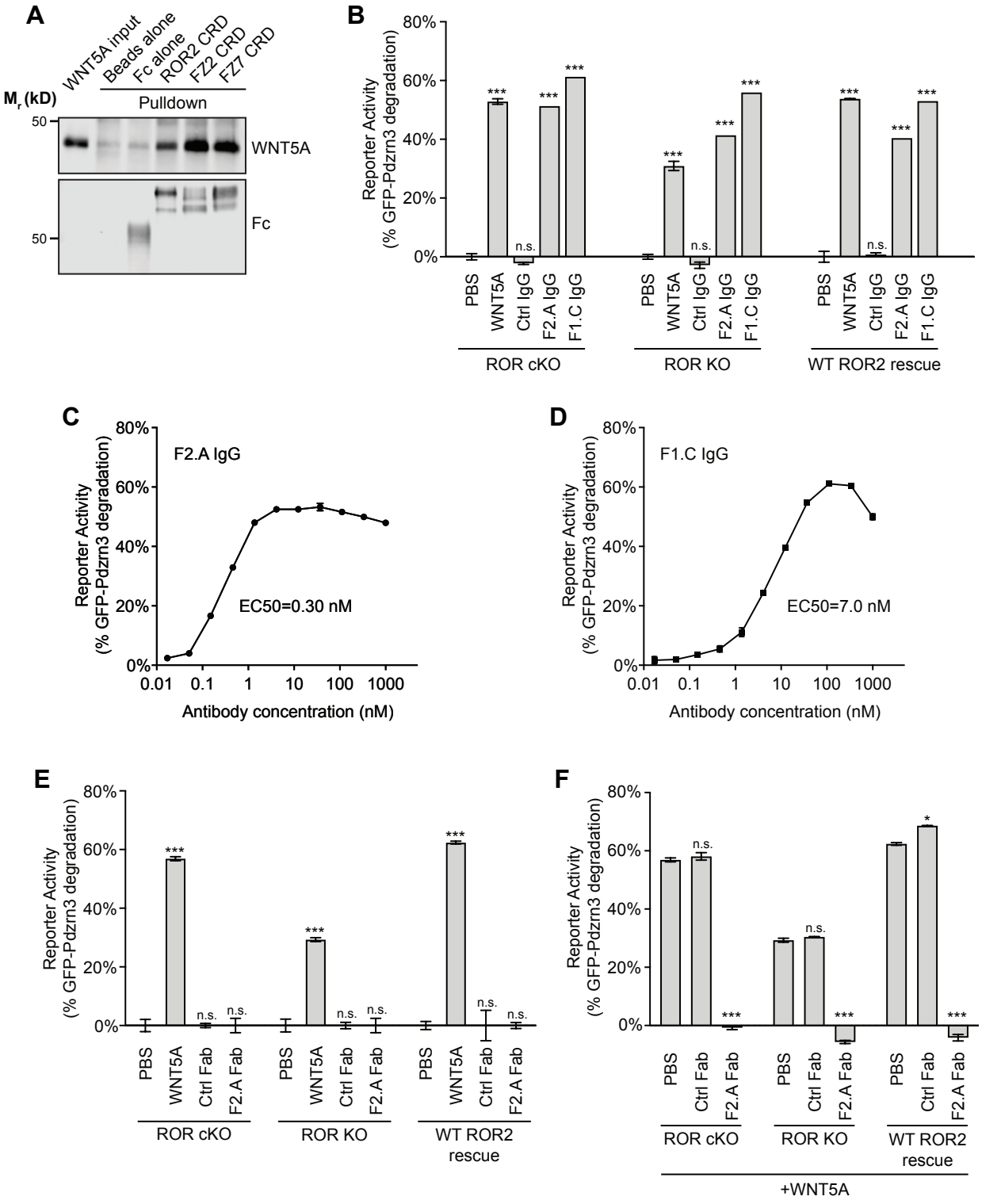
A
WNT5A input
Beads alone
Fc alone
ROR2 CRD
FZ2 CRD
FZ7 CRD
Pulldown
M_r (kD)
50
WNT5A
Fc
B
Reporter Activity
(% GFP-Pdzrn3 degradation)
80%
60%
40%
20%
0%
***
n.s.
PBS
WNT5A
Ctrl IgG
F2.A IgG
F1.C IgG
ROR cKO
ROR KO
WT ROR2 rescue
C
F2.A IgG
EC50=0.30 nM
Antibody concentration (nM)
0.01
0.1
1
10
100
1000
D
F1.C IgG
EC50=7.0 nM
E
Ctrl Fab
F2.A Fab
WT ROR2 rescue
F
*
+WNT5A

Figure 4-figure supplement

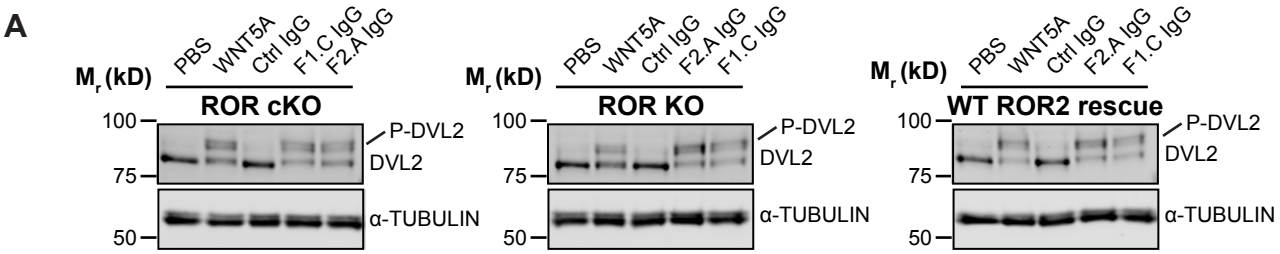

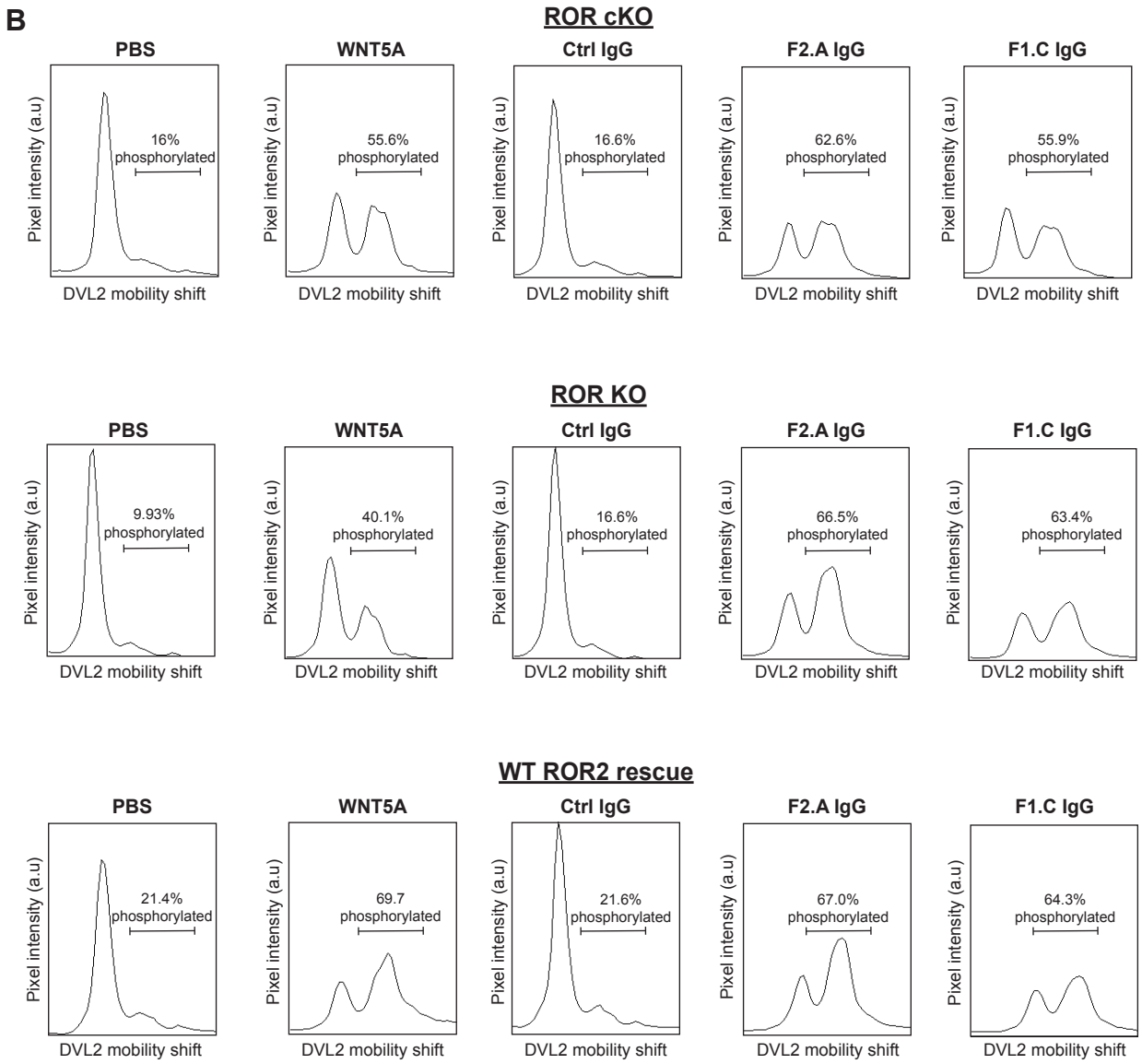

Figure 5

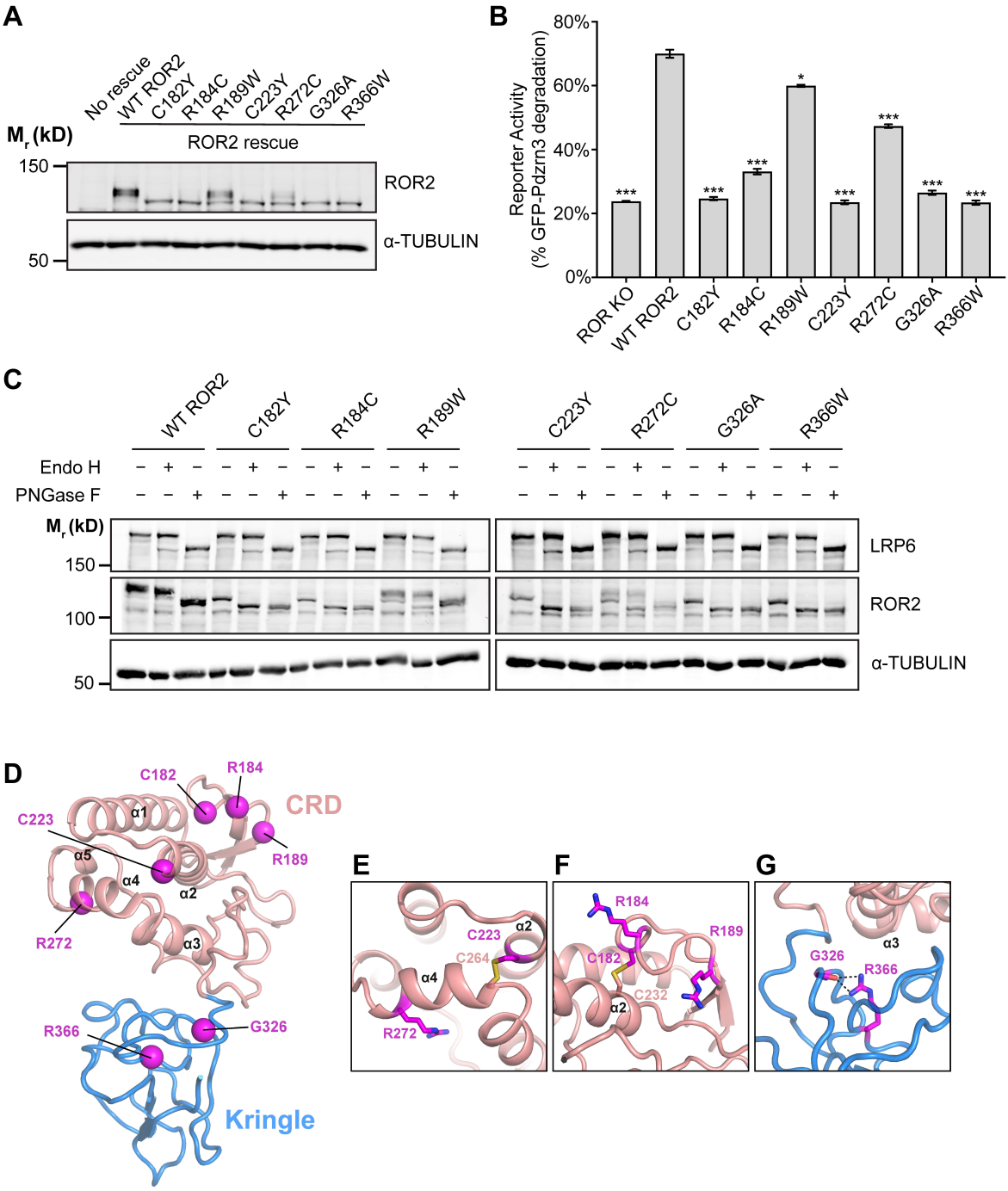
A
No rescue
WT ROR2
C182Y
R184C
R189W
C223Y
R272C
G326A
R366W
ROR2 rescue
M_r (kD)
150
50
ROR2
α-TUBULIN
B
Reporter Activity
(% GFP-Pdzrn3 degradation)
80%
60%
40%
20%
0%
ROR KO
WT ROR2
C182Y
R184C
R189W
C223Y
R272C
G326A
R366W
C
Endo H
PNGase F
M_r (kD)
150
100
50
LRP6
ROR2
α-TUBULIN
D
C182
R184
CRD
C223
α1
α5
α4
α2
R189
R272
α3
R366
G326
Kringle
E
C223
α2
C264
α4
R272
F
R184
R189
C182
C232
α2
G
G326
α3
R366

Figure 5-figure supplement 1

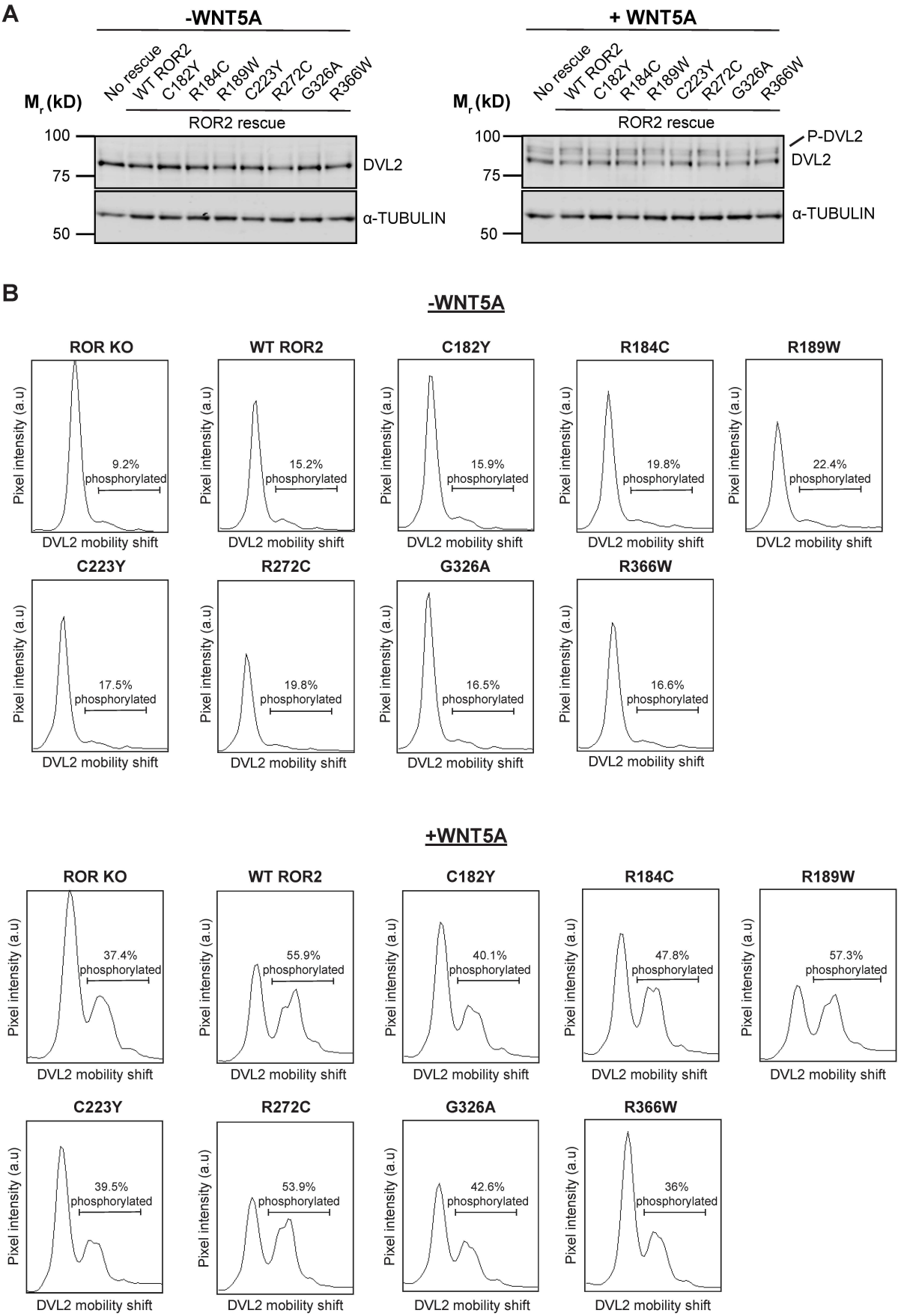

Figure 5-figure supplement 2

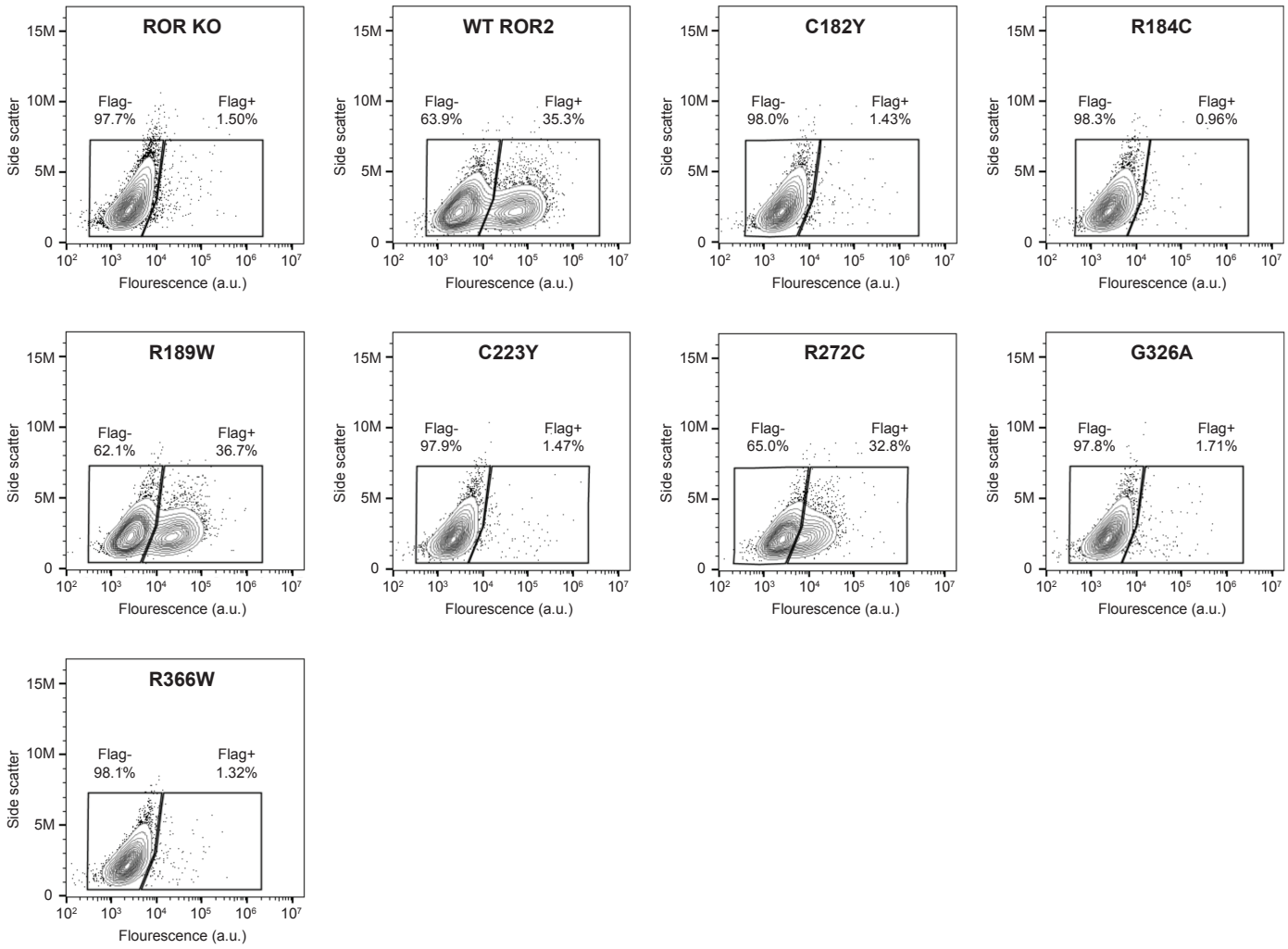

Figure 6

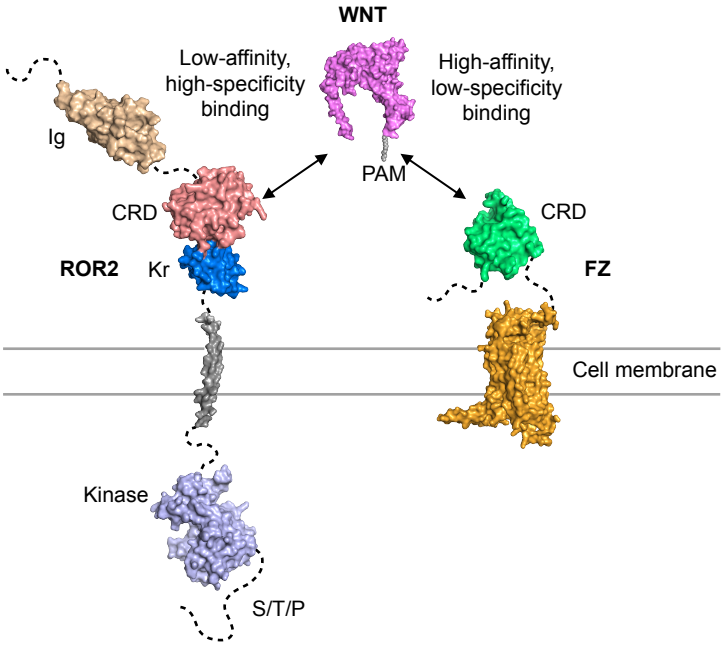
WNT
Low-affinity,
high-specificity
binding
High-affinity,
low-specificity
binding
Ig
PAM
CRD
CRD
ROR2
Kr
FZ
Cell membrane
Kinase
S/T/P